Physics of Fluids

Design optimization for Richtmyer-Meshkov instability suppression at shock-compressed material interfaces

Accepted Manuscript: This article has been accepted for publication and undergone full peer review but has not been through the copyediting, typesetting, pagination, and proofreading process, which may lead to differences between this version and the Version of Record.

Cite as: Physics of Fluids (in press) (2022); https://doi.org/10.1063/5.0100100
Submitted: 20 May 2022 • Accepted: 15 July 2022 • Accepted Manuscript Online: 18 July 2022

Dane M. Sterbentz, Charles F. Jekel, Dan White, et al.

View Online
Export Citation
CrossMark

APL Machine Learning
Open, quality research for the networking communities
Now Open for Submissions
LEARN MORE

AIP Publishing

Accepted to Phys. Fluids 10.1063/5.0100100

Physics of Fluids

Design optimization for Richtmyer–Meshkov instability suppression at shock-compressed material interfaces

Dane M. Sterbentz,[a] Charles F. Jekel, Daniel A. White, Sylvie Aubry, Hector E. Lorenzana, and Jonathan L. Belof[b]
Lawrence Livermore National Laboratory, Livermore, CA 94550, USA

(Dated: 8 July 2022)

The Richtmyer–Meshkov instability (RMI) is a phenomenon that occurs at the interface of two substances of different densities due to an impulsive acceleration, such as a shock wave passing through this interface. Under these conditions, the instability can be seen as interface perturbations begin to grow into narrow jets or spikes of one substance that propagate into the other. In some cases, this interface may involve an elastic-plastic material, which can play a significant role in the development and behavior of the RMI. The ability to effectively control RMI jetting and spike growth is one major limiting factor in technological challenges, such as inertial confinement fusion, that involve using high-pressure shock waves to implode a fuel target. The propagation of RMI growth can lead to increased asymmetry in this implosion process and significantly reduce the obtained energy yield. We use hydrodynamics simulations of impactor shock-compression experiments and methods based in design optimization to suppress RMI spike growth by altering the geometry and other properties of a shock-compressed elastic-plastic material target that shares an interface with atmospheric air. These hydrodynamics simulations use an arbitrary Lagrangian–Eulerian method with a high-order finite element approach. Our results demonstrate that RMI suppression can be achieved by intentionally creating a separate upstream interface instability to counteract the growth of long narrow RMI spikes at an interface with initial perturbations.

Keywords: Richtmyer–Meshkov instability, dynamic compression, optimization, shock waves

I. INTRODUCTION

The interface between two distinct fluids of different densities is generally conducive to the generation of unstable fluid motion. For the specific case in which this interface is impulsively accelerated (e.g., from the passage of a shock wave), this unstable fluid motion is referred to as the Richtmyer–Meshkov instability (RMI). Under these conditions, perturbations in the interface begin to grow due to the RMI, which leads to the propagation of jets or spikes of the denser substance into the fluid of lower density. RMI is prevalent in both natural processes, such as supernova explosions[1,2], as well as in technological settings such as inertial confinement fusion (ICF) applications[3–7]. The burning plasma that was recently produced by Zylstra et al.[7] in their landmark study represents a major step forward in the field of ICF. However, there are still several major challenges involved in attaining self-sustaining fusion energy. One major challenge encountered in ICF experiments, which generally use high-pressure shock waves to compress a fuel target, is asymmetry from mixing of the fuel with the surrounding capsule material during the implosion process. This mixing is often caused by instabilities such as RMI, which can be seeded by imperfections in the fuel capsule. The mixing of fuel with the surrounding capsule material can significantly reduce the energy yield of these experiments. Thus, the suppression of perturbation growth caused by RMI is an important, yet challenging, goal.

In many applications, the denser substance at the interface of interest may be an elastic-plastic material (i.e., a solid). Under high stresses and strain rates, a solid can significantly deform and exhibit fluid-like behavior, which includes the development of instabilities such as RMI. For RMI at interfaces that initially involve a solid, the elasticity and yield strength of the solid can play a major role in the propagation of RMI spike growth. At a certain point, material elasticity and strength can stabilize the RMI and arrest further spike growth[8]. Under certain circumstances, RMI spike growth may continue until these spikes rupture and form ejecta. The extreme pressure and temperature changes that occur during shock-wave compression can also lead to phase transitions (e.g., melting), which may further complicate unstable RMI behavior. Several experimental studies have investigated RMI involving a solid material to study material properties at extreme pressures and strain rates[9–12]. Theoretical and computational studies have also been conducted to provide a mechanistic understanding of RMI involving elastic-plastic materials. The landmark work of Piriz et al.[8] describes an analytical model for characterizing RMI growth at solid–vacuum interfaces. Their model provides scaling laws for predicting the maximum amplitude growth of the RMI spikes and showed that this amplitude is inversely proportional to the yield stress of the solid material. Dimonte et al.[13] built on the work of Piriz et al. by developing a scaling law for predicting RMI spike amplitude growth. This scaling law can also be used to infer the yield stress of a material by measur-

---

[a] Electronic mail: sterbentz2@llnl.gov
[b] Electronic mail: belof1@llnl.gov

Accepted to Phys. Fluids 10.1063/5.0100100

ing the RMI spike amplitude growth. The more recent work of Chen et al.[14] provides an analytical description of the dependency of elastic–plastic RMI perturbation growth on the Atwood number, a dimensionless number that describes the relative densities of the materials at the interface (we describe the Atwood number in more detail in the Methodology section of this paper).

These experimental and theoretical studies help provide a mechanistic understanding of RMI involving elastic–plastic materials occurring under various conditions. However, an effective method for suppressing RMI perturbation growth remains difficult to achieve. Several methods have previously been proposed for suppressing RMI perturbation growth. These include using magnetic fields to stabilize the RMI and prevent perturbation growth[15–17] when a plasma is present at the interface. Alternatively, Sano et al.[18] propose using a density transition layer at the interface to suppress RMI. This density transition layer provides a continuous transition between the densities of the materials at the interface and appears to be effective at suppressing perturbation growth if a sufficiently thick transition layer is used. These methods for suppressing RMI perturbation growth tend to require specific conditions to be present and are not necessarily applicable to all applications involving RMI. Several recent studies, such as those of Henry de Frahan et al.[19], Feng et al.[20], and Liang et al.[21–23] have investigated RMI in scenarios involving several layers of different density fluids with coupled interfaces. These studies have focused on analyzing the effect of upstream interfaces with perturbations that create reverberating shock waves inside the fluid layers and have found that RMI and other hydrodynamic instabilities can be enhanced or suppressed in this manner.

For this study, we propose using a shape optimization approach[24] to reduce or suppress the RMI spike growth of a solid target material (with an initially perturbed surface in contact with atmospheric air) undergoing shock-wave compression. Our design optimization focuses on modifying the geometry of the target that is upstream of the initially perturbed interface where the primary RMI spike growth occurs. Note that we do not simply alter the geometry of the initially perturbed interface, as it may not be possible or practical to alter this interface in various engineering applications. For instance, this perturbed interface may arise in an engineering scenario from a limitation in manufacturing methods or may have desirable properties for a specific application. Our computational study demonstrates that reduction and partial suppression of RMI spike growth is achievable under specific conditions. The optimized designs that we have developed suppress RMI perturbation growth by intentionally generating another RMI that occurs upstream of the initially perturbed interface, which appears to counteract unstable spike growth at the interface of interest. We refer to this intentionally produced RMI as the rectifying RMI. We also investigate the underlying dynamics of why our optimized designs are effective at suppressing RMI spike growth by considering shock-wave behavior (such as reverberating shock waves) and vorticity deposition in the target material.

II. METHODOLOGY

A. Richtmyer–Meshkov instability characteristics

In this section, we describe several characteristics of the RMI that are important for understanding the methods that we use for suppressing this instability. We consider the case where the impulsive acceleration that generates the RMI is caused by an incident shock wave moving in a normal direction to the initially perturbed interface (i.e., the x-direction in Figure 1). One common description of the mechanism that leads to RMI perturbation growth comes from considering vorticity deposition $\vec{\omega}$ as the incident shock wave refracts at the perturbed interface. Note that vorticity represents the curl of the velocity vector (i.e., $\vec{\omega} = \nabla \times \vec{u}$). This vorticity deposition generates counterclockwise (positive) vorticity on one side of an interface perturbation and clockwise (negative) vorticity on the other side of the perturbation (see diagrams in Figure 1)[25,26]. This vorticity imbalance causes the interface perturbations to deform, leading to RMI perturbation growth. For single-mode perturbations, this perturbation growth generally occurs as long narrow jets or spikes with a rounded bubble structure in between these spikes as shown in Figure 1.

The general behavior of RMI perturbation growth at an interface is strongly dependent on a dimensionless ratio known as the Atwood number. The Atwood number quantifies the difference in density between the two interface substances prior to shock loading and is defined as[14,26]

$$A = \frac{\rho_2 - \rho_1}{\rho_2 + \rho_1}, \tag{1}$$

where ρ_1 is the density of the upstream material through which the shock wave is initially moving and ρ_2 is the density of the other substance or material at the interface. If the magnitude of the Atwood number is close to unity (i.e., $|A| \approx 1$, which is the case for solid–vacuum interfaces), this indicates a large difference in the density of the two substances or materials. If the magnitude of the Atwood number is close to zero (i.e., $|A| \approx 0$), the densities of the materials are approximately equal and this generally represents a more stable configuration. The developmental behavior of RMI spike growth is dependent on the Atwood number. For instance, if $A > 0$, then the interface perturbation spikes simply grow in the x-direction toward the lower-density material as shown in Figure 1(a). However, if $A < 0$, a phase inversion occurs as the perturbations begin to deform as shown in Figure 1(b) and it is these phase-inverted spikes that grow into the lower-density material[26]. For our analysis, we focus on suppressing RMI spike growth in scenarios where

Accepted to Phys. Fluids 10.1063/5.0100100

the density of the upstream material ρ_1 is significantly greater than the density of the other substance at the interface ρ_2 (i.e., scenarios where $A \approx -1$).

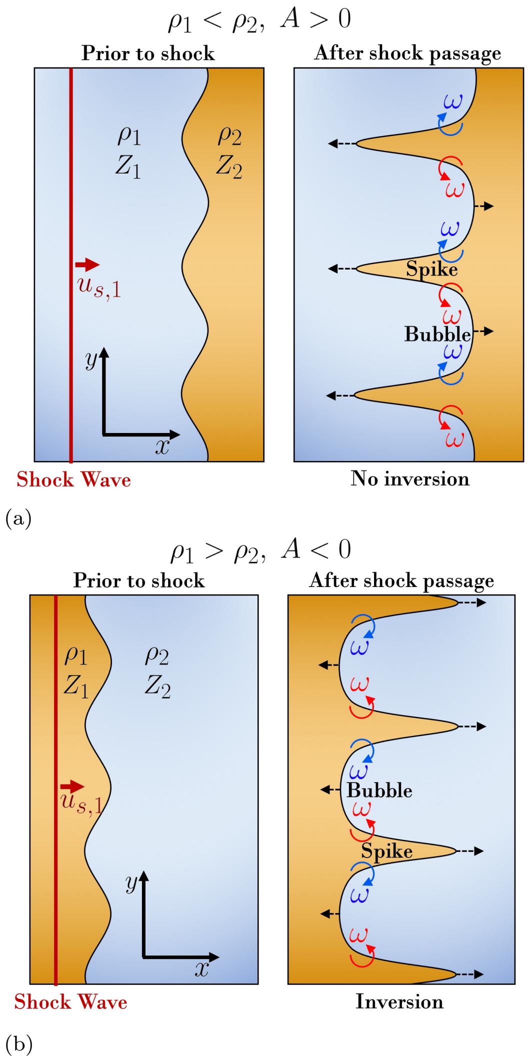

FIG. 1: The unstable behavior at the interface (due to the RMI) is highly dependent on the relative densities between the materials at the interface, which is encapsulated in the dimensionless Atwood number A [see definition in Equation (1)]. For both cases, spikes of the denser material propagate in the x-direction toward the less dense material. If $A > 0$, no inversion of the interface perturbations occurs. Note that the curled arrows represent the general direction of the vorticity $\vec{\omega}$, which plays a major role in RMI spike growth. The variables ρ, Z, and u_s are the initial density (prior to shock loading), shock impedance, and shock velocity magnitude, respectively: (a) Atwood number is positive ($A > 0$) and no perturbation inversion occurs after shock wave passage; (b) Atwood number is negative ($A < 0$) and a perturbation inversion occurs.

Additionally, the shock impedance of the materials at the interface plays a crucial role in the shock-wave behavior and corresponding vorticity deposition. The shock impedance of a given material is defined as $Z = \rho_i u_s$, where ρ_i is the initial density (prior to shock loading) of the material and u_s is the shock velocity magnitude within the material. According to Nellis et al.[27], if we define Z_1 as the impedance of the upstream material (through which the shock wave is initially moving) and Z_2 as the impedance of the downstream material, then the following is true. If $Z_1 < Z_2$, then the shock wave is at least partially reflected when it reaches the interface between the two materials and reverberates back through material Z_1 at higher pressure. Otherwise, if $Z_1 > Z_2$, then a rarefaction wave is produced in material Z_1 when the shock wave reaches the interface and the pressure is isentropically released. This concept will be important in understanding the shock-wave behavior and corresponding vorticity deposition for our results in Section III.

B. Simulation setup

The simulation setup that we consider in our analysis involves a high-velocity copper impactor striking a stationary copper target to generate a shock wave that passes through the target. We generally use an impactor velocity of $V_i = 0.2$ cm/μs in our simulations. The copper target is in contact with air on the side of the target opposite to the side where the impact occurs [see diagram in Figure 2(a)] and has an Atwood number of $A \approx -1$. For convenience, we will henceforth refer to the side of the target struck by the impactor as the left-hand side and to the opposite side of the target as the right-hand side. The right-hand side of the target includes non-smooth perturbations along the interface with the air. For these initial perturbations, we have chosen to use a periodic single-mode sinusoidal profile. During compression, these perturbations first invert phase and then begin to grow after the shock passes through the copper–air interface on the right-hand side of the target. The conditions chosen for these simulations are similar to gas-gun dynamic-compression experiments being conducted at the High Explosives Application Facility (HEAF) at Lawrence Livermore National Laboratory (LLNL) and the Dynamic Compression Sector user facility at Argonne National Laboratory[28,29]. These experiments are currently ongoing and will be published in a future article.

The dimensions of the copper impactor and target in our simulations are listed in Table I. Note that in our simulations, we use $N_r = 10$ perturbation periods on the right-side of the target and zero-velocity (rigid wall) boundary conditions in the y-direction on the top and bottom sides of our simulation domain. While we could also have used periodic boundary conditions with $N_r = 1$ in our simulations, we wanted to investigate potential edge effects. However, we found the edge effects to be largely negligible in our simulations (see simulation density plot in Figure 3). For this reason, we only

Accepted to Phys. Fluids 10.1063/5.0100100

TABLE I: Dimensions of impactor–target setup used in our two-dimensional simulations.

Dimension	[mm]
Setup Diameter	45.0
Impactor Thickness	10.0
Target Thickness	5.0
Perturbation Amplitude	0.5
Perturbation Period	4.5

show a reduced number of perturbation periods (e.g., $N_r = 2$) for our simulation results in Section III. For the left and right sides of our simulation boundaries, we use zero-velocity boundary conditions in both the x- and y-direction.

Our two-dimensional simulations are constructed using the hydrodynamics code MARBL[30,31], developed at LLNL, which numerically solves the conservation of mass, momentum, and energy equations. MARBL is an arbitrary Lagrangian–Eulerian code that uses a high-order finite element approach to increase accuracy of the numerical calculations[32]. For the materials in our simulations, we use the Livermore Equation of State (LEOS) library, which was also developed at LLNL. The material equations of state for copper, air, and lucite (a low-density plastic resin that we use in some of our simulations) come from LEOS tables 290[33], 2260, and 5070, respectively. They are based on the quotidian equation of state with extension formalism[34,35]. For copper, we use the Steinberg–Guinan strength model[36] with a shear modulus of 0.477 Mbar, an initial yield stress of 1.2×10^{-3} Mbar, and a maximum work hardening stress of 6.4×10^{-3} Mbar. We neglect the strength of lucite in our simulations.

For the hydrodynamics simulations used in our study, we use a largely uniform mesh of approximately 83,000 elements with a grid spacing of $\Delta x = 0.0208$ cm in both the x- and y-directions. We found a maximum difference of only approximately 2% between the RMI spike growth at this mesh resolution and at higher resolutions, which indicates that our simulations are largely converged. In Appendix A, we also compare simulation results using this setup to the scaling law developed by Dimonte et al.[13] to demonstrate that the material models we use (e.g., the strength and failure models for the copper impactor and target) are accurately capturing the RMI behavior in the high-pressure regimes that we consider.

C. Design parameterization

Now that we have described our simulation setup, we outline the methodology that we use for reducing and suppressing RMI spike growth. For our study, we focus

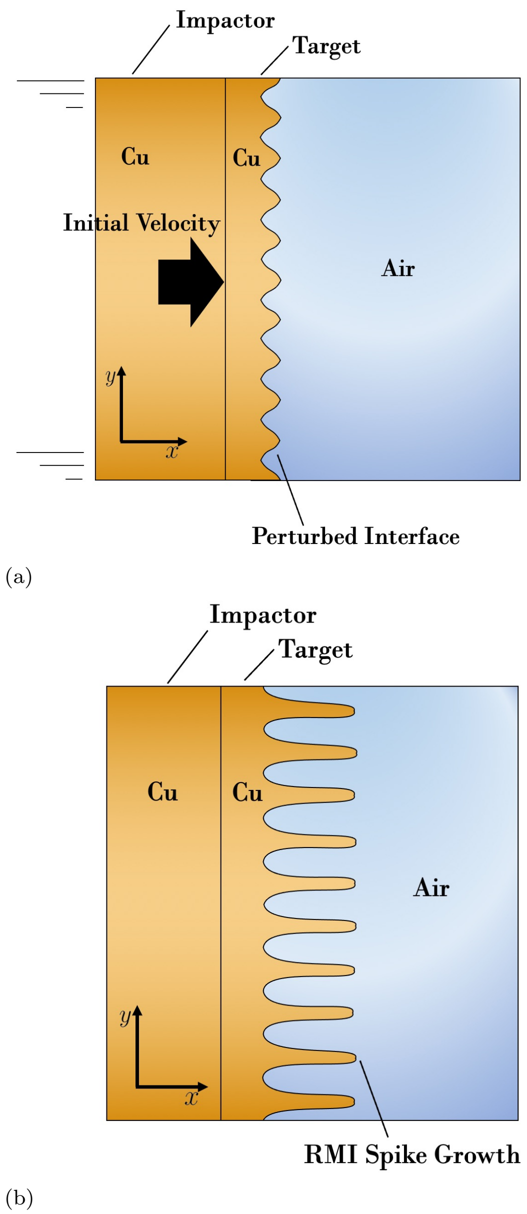

FIG. 2: The simulation setup used in our analysis. A high-velocity impactor is launched toward a copper target with a given initial velocity. This impact generates a shock wave that passes through the target, which has a perturbed interface on the right-hand side: (a) The initial configuration of the setup showing the perturbed interface just prior to impact; (b) After the shock wave passes through the perturbed interface, the RMI leads to an inversion of the troughs of the perturbed interface, which then begin to grow into thin spikes. The peaks of the initially perturbed interface form into structures that we refer to as bubbles.

Accepted to Phys. Fluids 10.1063/5.0100100

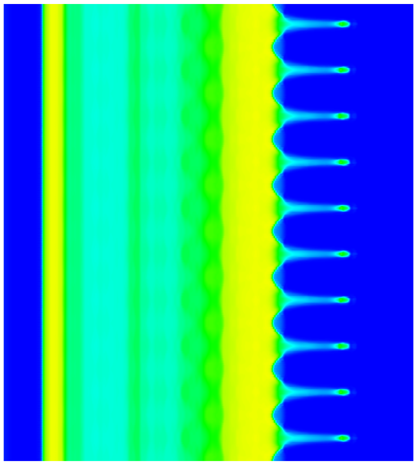

FIG. 3: Density plot for the baseline simulation that we use in our analysis at 7 μs after the impact occurs. This plot shows RMI spike growth for all $N_r = 10$ periods used in our simulation. As is clear from the plot, the RMI spikes near the upper and lower edge of the simulation domain appear to be unaffected by any edge effects due to the zero-velocity boundary conditions.

on investigating designs that involve modifying the geometry of the left-hand side of the target. This allows us to tune the dynamics of the shock wave and response of the target material to the shock wave. The geometry of the right-hand side of the target, which includes the initial perturbations that seed the RMI, remains unchanged in our simulations. As previously discussed, it may be necessary or unavoidable for a specific engineering application to have these perturbations, but highly undesirable for RMI spike growth to occur because of these perturbations.

One promising parameterization that we have developed is to use piecewise cubic Hermite interpolating polynomials (PCHIP) to shape the geometry of the left-hand side of the target. For this parameterization, we select several equidistant adjustment points along the axis parallel to the left-hand side of the target (i.e., the y-direction) $y_k,\ k = 0, 1, 2, \cdots, N$ as well as corresponding x-direction values at these points $f(y_k) = f_k$. Between these adjustment points, we interpolate using a polynomial equation of the following form

$$\begin{aligned} f(y) = H_{00}(t)f_k + H_{10}(t)(y_{k+1} - y_k)f'_k \\ +H_{01}(t)f_{k+1} + H_{11}(t)(y_{k+1} - y_k)f'_{k+1} \end{aligned} \tag{2}$$

where $t = (y - y_k)/(y_{k+1} - y_k)$ and $H_{ij}(t)$ are Hermite basis functions and are defined as

$$\begin{aligned} H_{00}(t) &= 2t^3 - 3t^2 + 1, \\ H_{10}(t) &= t^3 - 2t^2 + t, \\ H_{01}(t) &= -2t^3 + 3t^2, \\ H_{11}(t) &= t^3 - t^2. \end{aligned} \tag{3}$$

In Equation (2), the f'_k term represents the slope at each of the points y_k. For our application, we have chosen to preserve monotonicity between the y_k points using the method developed by Fritsch and Carlson[37] and set this slope equal to

$$f'_k = \frac{w_1 + w_2}{(w_1/d_{k-1}) + (w_2/d_k)} \tag{4}$$

where $h_k = y_{k+1} - y_k$ and $d_k = (x_{k+1} - x_k)/h_k$ represents the internal slopes at each point y_k. The variables w_1 and w_2 are weighting factors and are set equal to $w_1 = 2h_k + h_{k-1}$, and $w_2 = h_k + 2h_{k-1}$. If the slopes d_k and d_{k-1} are opposite in sign or one of them is equal to zero, then f'_k is simply set equal to zero.

Using the selected adjustment points y_k, the corresponding values f_k, and interpolating between these points using Equations (2) and (4), we can construct a half wavelength profile, which can then be mirrored to produce a full wavelength profile. This profile is then repeated to produce a periodic interface on the left-hand side of the target, which we refer to as a PCHIP profile. Figure 4 shows what a single period of a potential PCHIP profile may look like for four y_k points. This allows us to create a periodic wave profile that can achieve many different wave profile shapes that depend on the values chosen for f_k. The PCHIP profile also preserves monotonicity between the y_k points and is first derivative continuous. An alternative parameterization method that we have also tried is to interpolate between the adjustment points y_k using simple linear interpolation rather than PCHIP polynomials. Piecewise linear interpolation produces a less complex profile on the left-hand side of the target that is simpler to manufacture using standard machine tools (e.g., for an experiment) because it only uses straight lines to produce the profile. We show an optimized result in Section III that uses piecewise linear interpolation in addition to results that use PCHIP interpolation.

Note that these profiles create gaps or cavities between the target and the impactor (see Figure 4) that can be filled with either air or another material. We typically fill these cavities in our simulations using lucite, a low-density plastic resin, that helps maintain numerical stability. However, the difference in the final results between using air or lucite to fill these cavities is generally small.

Using the PCHIP profile (or alternatively the piecewise linear profile), we can select several parameterizations to generate our design space. For our study, we adjust four values [i.e., $f(y_0)$, $f(y_1)$, $f(y_2)$, and $f(y_3)$] and the number of periods on the left-hand side of the target N_l (or equivalently the wavelength of the repeated profile). Note that we equidistantly space the four points y_k such that they span an entire half period. This creates a total of five parameters for our design space that can be optimized to reduce or suppress RMI spike growth.

Accepted to Phys. Fluids 10.1063/5.0100100

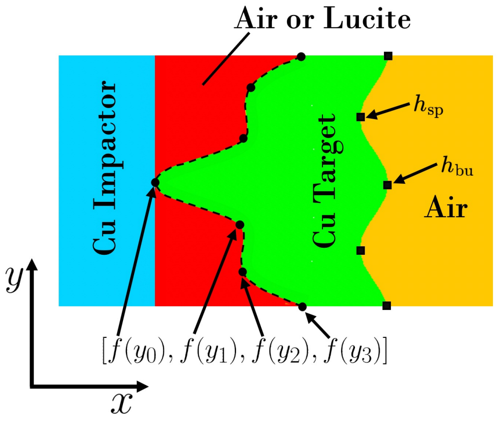

(a)

FIG. 4: The PCHIP profile is created by selecting values $f(y_k)$ corresponding to each of the adjustment points y_k and interpolating between these points to create a smooth, first-derivative continuous profile. We use four adjustment points (i.e., y_0, y_1, y_2, and y_3) to create this profile. The PCHIP profile is applied to the left-hand side of the target (i.e., the side struck by the copper impactor). We place tracer particles on the right-hand side of the target to measure the spike amplitude h_{sp} and bubble amplitude h_{bu}. We use these amplitudes to quantify RMI spike growth using the objective function of Equation (5). The materials used in our simulations are also labelled in the figure diagram. The cavities (created by the PCHIP profile) between the impactor and target are filled with either air or another material. We use lucite plastic resin to fill this space in our simulations.

D. Design optimization problem

For the design optimization analysis, we must first define a performance metric or objective function that we intend to minimize such that RMI spike propagation is reduced or suppressed. One objective function that we have selected for this purpose is

$$\phi = \frac{1}{N_r} \sum_{i=1}^{N_r} |h_{\mathrm{sp},i} - h_{\mathrm{bu},i}|, \tag{5}$$

where N_r is the number of periods of the initial perturbations on the right-hand side of the target, $h_{\mathrm{sp},i}$ is the amplitude of the i-th RMI spike, and $h_{\mathrm{bu},i}$ is the amplitude of the i-th RMI bubble. The initial locations of the tracer particles that we use to determine $h_{\mathrm{sp},i}$ and $h_{\mathrm{bu},i}$ are shown in Figure 4. The objective function in Equation (5) represents an average amplitude difference between RMI spikes and bubbles across all perturbation periods and is useful for ensuring that the right-hand side of the target is as flat as possible at a specified time.

For certain applications, it may be desirable to not only ensure that RMI spike propagation is suppressed, but also that the target remains as compact as possible. For this purpose, we have also investigated another objective function that is useful for maintaining target compactness by quantifying the deviation from the target's center-of-mass, which is computed via

$$\Phi = \left[\int_{\Omega_T} \rho\left(x\right) \left(x - x^*\right)^p \right]^{1/p} \tag{6}$$

where ρ denotes the material density at point x and x^* denotes the center-of-mass. The integral is computed only over the target material Ω_T. We use a value of $p = 6$, which can be considered a soft-max function (i.e., a smooth estimate of the maximum deviation of material about the center-of-mass). A diagram of the properties that we use in the objective function of Equation (6) is illustrated in Figure 5. This new metric does not utilize tracers as in the objective function of Equation (5), but rather it requires images of material density to be saved to disk and post-processed. This post-processing involves determining the x location for some finite-sized volume of the target and the corresponding density $\rho(x)$ of this volume. This is repeated to cover the entire target volume Ω_T, which allows us to calculate the integral of Equation (6).

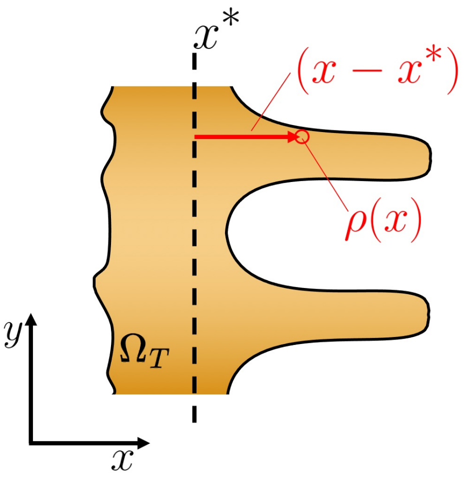

FIG. 5: The properties used in the calculation of the target compactness metric of Equation (6). The center-of-mass (in the x-direction) of the target x^* is calculated first. The location x and density $\rho(x)$ at finite-sized volumes throughout the target are then determined to compute the integral in Equation (6) over the entire target domain Ω_T as explained in the text.

The objective of our optimization is to find the design that minimizes the objective function [i.e., either Equation (5) or Equation (6)] at a specific time Δt after the impactor strikes the target or minimizes the maximum objective function value over a specified time duration (e.g., between 0 μs and 7 μs after impact). We have somewhat arbitrarily set $\Delta t = 7$ μs as the final time in our analysis. This allows sufficient time for the

Accepted to Phys. Fluids 10.1063/5.0100100

shock wave to pass through the perturbed interface on the right-hand side of the target and additional time for RMI spike growth to occur. Another reason that we have chosen to set the final simulation time equal to $\Delta t = 7$ μs is because the in-progress independent experiments on which our simulation setup is based generally take measurements up until approximately 7 μs after the impactor strikes the target.

Our design optimization problem is largely defined by a mapping between the parameterization of Equation (2) and the objective function of either Equation (5) or Equation (6). We presume that this is a smooth, but not necessarily convex, mapping. The design optimization problem is unconstrained other than simple bounds on the design parameters. We chose the search bounds for the PCHIP parameters to be within the range $f(y_n) \in [-0.25 \text{ cm}, 0.25 \text{ cm}]$. These bounds correspond to a distance from the left-hand side of the target and were chosen to be sufficiently small to prevent the target from becoming too thin and rupturing during the RMI spike growth phase of the simulation. The parameter bounds for the number of periods of the profile on the left-hand side of the target is within the range $N_l \in [0.25, 2]N_r$ where N_r is the number of periods on the initially perturbed right-hand side of the target. In summary, our optimization problem can be written in the standard optimization formula as

$$\begin{aligned} \min_{f_0,f_1,f_2,f_3,N_l} \quad & \phi \text{ or } \Phi \\ \text{subject to} \quad & -0.25 \text{ cm} \le f(y_0) \le 0.25 \text{ cm} \\ & -0.25 \text{ cm} \le f(y_1) \le 0.25 \text{ cm} \\ & -0.25 \text{ cm} \le f(y_2) \le 0.25 \text{ cm} \\ & -0.25 \text{ cm} \le f(y_3) \le 0.25 \text{ cm} \\ & N_r/4 \le N_l \le 2N_r . \end{aligned} \tag{7}$$

We apply a gradient-free design optimization algorithm known as differential evolution optimization (DEO) to the optimization problem defined in Equation (7), which is described further in Appendix B.

III. RESULTS AND DISCUSSION

A. RMI suppression

We use a hierarchical optimization process that involves two primary stages where a set of parameters are optimized using the DEO algorithm. The first DEO stage involves identifying which of the five parameters [i.e., N_l, $f(y_0)$, $f(y_1)$, $f(y_2)$, $f(y_3)$] play a dominant role in reducing the objective function and which parameters can simply be set equal to a boundary value. From the first DEO stage, we found that using $N_l = N_r/2$ is generally the most effective for suppressing RMI spike growth. For most of our design optimization processes, we also found that setting $f(y_0)$ and $f(y_3)$ equal to the minimum and maximum bounds, respectively [i.e., $f(y_0) = -0.25$ cm and $f(y_3) = 0.25$ cm], appears to be effective for reducing RMI spike growth. This leaves us with only two parameters for the second optimization stage [i.e., $f(y_1)$ and $f(y_2)$] that we again optimize using the DEO algorithm. The number of parameters D, approximate number of DEO generations G, and approximate number of objective function ϕ evaluations for each DEO stage is summarized in Table II. Note that the number of objective function evaluations corresponds to the number of times the hydrodynamics simulation must be run.

TABLE II: The number of parameters D, approximate number of generations G, and approximate number of objective function ϕ evaluations for the two DEO stages of the hierarchical optimization process that we use.

DEO Stage	Parameters D	Generations G	Evaluations of ϕ $10 \cdot D \cdot (G+1)$
1	5	≈ 20	≈ 1050
2	2	≈ 15	≈ 320

We compare the optimized designs developed using this optimization hierarchy to the baseline case where the left-hand side of the target is completely flat. For all density plots that we show in this section, the density values map to the color bar shown in Figure 6. Figure 7 shows density plots for the baseline case at several time instants after the impactor strikes the target. Figure 7(a) displays the initial target configuration at the instant that it is struck by the impactor at $\Delta t = 0$ μs (just prior to deformation). After $\Delta t = 1.75$ μs, a phase inversion of the interface perturbations has clearly occurred as shown in Figure 7(b). At later times [see Figure 7(c)–(e)], the inverted perturbations continue to grow into long narrow spikes due to the RMI.

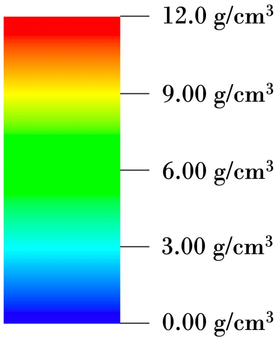

FIG. 6: The density values for the plots in Figures 7–11 map to the color bar in this figure, where blue represents the minimum density (0.00 g/cm^3) and red represents the maximum density (12.0 g/cm^3).

Our optimized designs aim to halt and suppress the significant RMI spike growth seen in Figure 7. Figure 8 shows density plots (at the same time instances after impact as in Figure 7) of one of our designs using

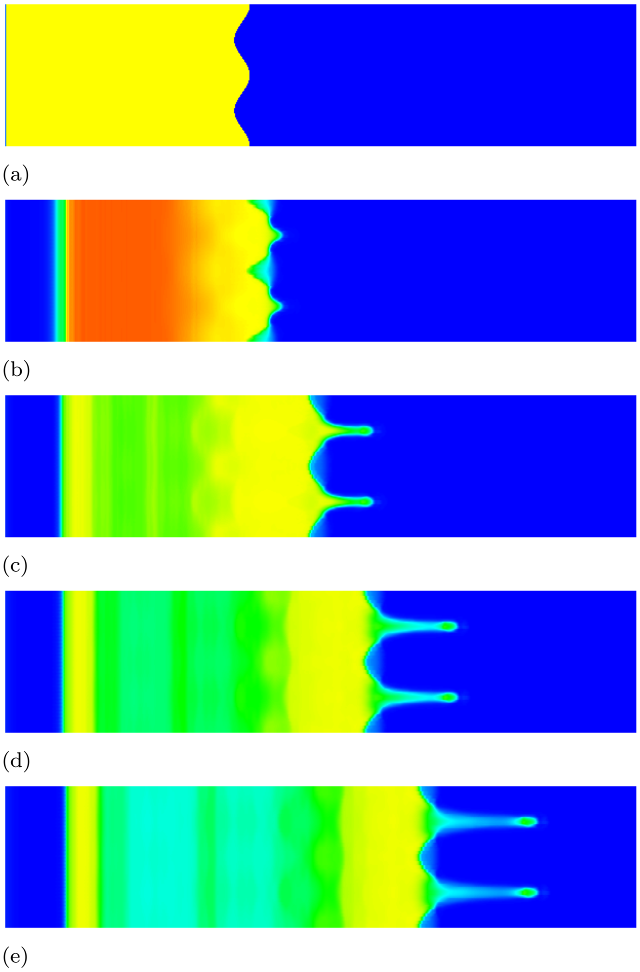

(a)

(b)

(c)

(d)

(e)

FIG. 7: Density plots at several time instants after the impactor strikes the target (baseline case with no RMI suppression). There appears to be fairly significant RMI spike growth: (a) $\Delta t = 0.0$ μs (initial configuration at impact); (b) $\Delta t = 1.75$ μs; (c) $\Delta t = 3.50$ μs; (d) $\Delta t = 5.25$ μs; (e) $\Delta t = 7.0$ μs.

the DEO algorithm to optimize the PCHIP parameters $f(y_1)$ and $f(y_2)$. Equation (5) is used as the objective function, where this function is minimized at $\Delta t = 7$ μs. The cavities created by the PCHIP profile are filled with lucite as previously mentioned. The PCHIP profile on the left-hand side of the target [see Figure 8(a)] creates an entirely new RMI, which we refer to as the rectifying RMI. This rectifying RMI is equivalent to a positive Atwood number (i.e., $A > 0$) RMI where no perturbation inversion occurs and the spikes grow left towards the impactor. The vorticity created by this new instability largely counteracts/overtakes the vorticity on the right-hand side of the target and halts or redirects RMI spike growth on this side of the target. We further investigate shock-wave behavior and vorticity deposition for our optimized designs in Section III E.

An alternative design is shown in Figure 9. The cavities between the RMI spikes on the right-hand side of the target [see Figure 9(c)] are “pinched” together by $\Delta t = 7$ μs. This leads to the largely flat interface seen in Figure 9(e). Similar to the design shown in Figure 8, the design in Figure 9 also uses the PCHIP parameterization on the left-hand side of the target and uses a form of the objective function of Equation (5). However, we make two modifications to the way that the objective function is evaluated. Instead of minimizing the objective function only at $\Delta t = 7$ μs, we minimize the maximum value of the objective function over the entire time duration between $\Delta t = 0$ μs and 7 μs. This helps maintain a relatively flat interface on the right-hand side of the target throughout the simulation. In evaluating the objective function of Equation (5), we also found it useful to use the average of every other tracer pair $i = 1, 3, 5, \ldots, N_r$ rather than the average of all tracer pairs $i = 1, 2, 3, \ldots, N_r$ as we did for the design in Figure 8. Using every other tracer pair appears to be more conducive to producing the “pinching” effect that we observe for the optimized design in Figure 9.

Another alternative optimized design that we have found to work well for suppressing RMI spike growth on the right-hand side of the target is shown in Figure 10. This design uses piecewise linear segments (instead of PCHIP) to produce the profile on the left-hand side of the target and involves using a layer of lucite between the impactor and the target [see Figure 10(a)]. We again use the DEO algorithm to optimize two parameters, which are the thickness of the lucite layer and the angle of the grooves on the left side of the target. The effect is similar to the designs in Figures 8 and 9 where a rectifying RMI is created with a positive Atwood number. As seen in Figure 10(e), this design is also fairly effective at suppressing RMI growth on the right-hand side of the target. Additionally, this design is relatively easy to manufacture using standard machine tools as previously discussed and is a good initial candidate for an experimental study.

B. Designing for target compactness

The above results illustrate that RMI, as defined by the objective function in Equation (5), can be reduced to near zero by optimizing the profile of the left-hand side of the target. Note, however, that the results in Figures 8–10 show that the left-hand side of the target becomes quite distorted as large bubbles form on this side of the target. This may be inappropriate for some applications. As a second design experiment, we investigate the target compactness objective function of Equation (6) in an attempt to both reduce RMI and also keep the target relatively compact.

In this new study, the target and impactor materials, dimensions, and initial velocities are identical to those in the previous study. Likewise, the same PCHIP parameterization is used on the left-hand side of the target. Note that in this study the area (and mass) of the target

Accepted to Phys. Fluids 10.1063/5.0100100

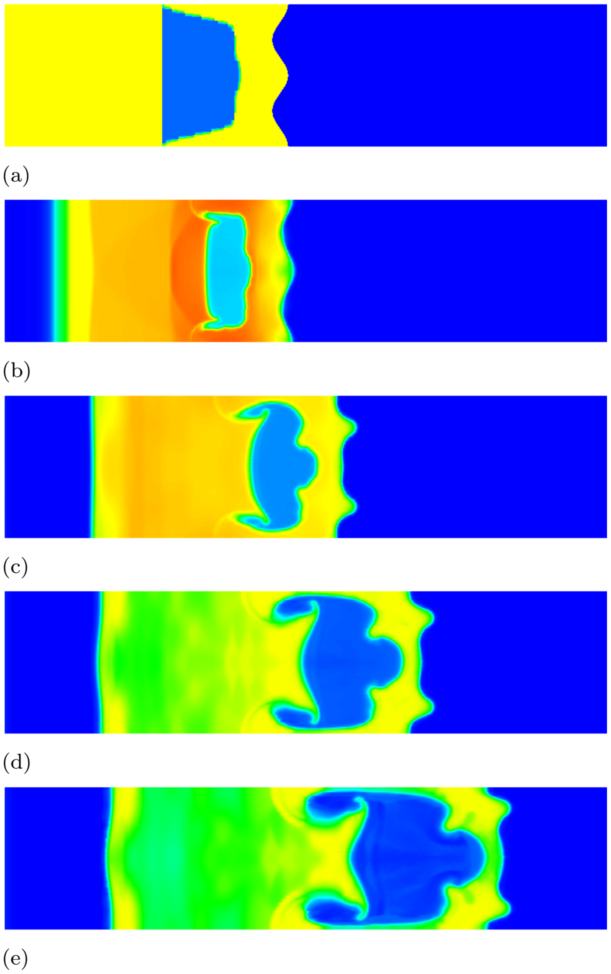

(a)

(b)

(c)

(d)

(e)

FIG. 8: Density plots at several time instants after the impactor strikes the target of an optimized design that uses the PCHIP parameterization on the left-hand side of the target. This design partially suppresses RMI spike growth on the right-hand side of the target: (a) $\Delta t = 0.0$ μs (initial configuration at impact); (b) $\Delta t = 1.75$ μs; (c) $\Delta t = 3.50$ μs; (d) $\Delta t = 5.25$ μs; (e) $\Delta t = 7.0$ μs.

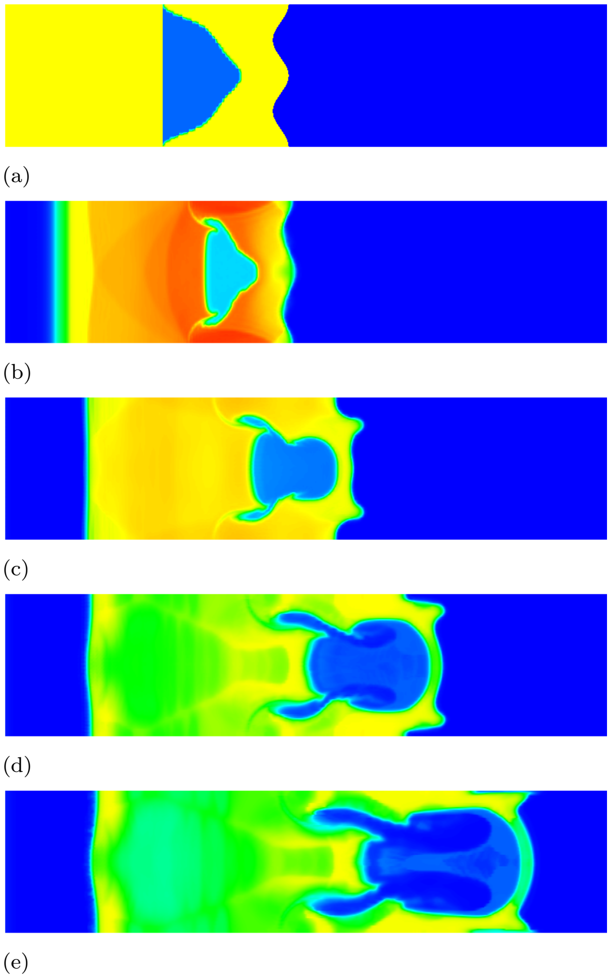

(a)

(b)

(c)

(d)

(e)

FIG. 9: Density plots at several time instants after the impactor strikes the target of an optimized design that uses a piecewise linear parameterization on the left-hand side of the target. The design in this figure uses a slightly modified objective function from that used to produce the results in Figure 8, as explained in the text. This design largely suppresses any significant RMI spike growth and creates a "pinching" effect [see plot in (e)] that produces a relatively flat interface on the right-hand side of the target: (a) $\Delta t = 0.0$ μs (initial configuration at impact); (b) $\Delta t = 1.75$ μs; (c) $\Delta t = 3.50$ μs; (d) $\Delta t = 5.25$ μs; (e) $\Delta t = 7.0$ μs.

is kept constant, meaning that the PCHIP polynomial coefficients are not independent because of a constraint on the area of the target. The DEO algorithm is again used to find the optimal design. The final design for this new study displays some interesting characteristics and is shown in Figure 11(a). The design has a low-amplitude high-frequency nature to it, which is quite different than the previous designs in Figures 8–10. The results at several other times are shown in Figure 11(b)–(e). The results in Figure 11 show that this design has reduced RMI spike formation compared to the baseline case in Figure 7, although the reduction is not as significant as that in Figures 8–10. The design in Figure 11 may also be difficult to manufacture due to its high-frequency nature. However, the left-hand side of the target no longer has large bubbles and the target is clearly more compact, which was the primary design objective.

C. Comparison of design results

Figure 12 provides a more quantitative comparison of the spike growth on the right-hand side of the target for the different designs in Figures 7–11 by plotting the difference between the spike amplitude and the bubble amplitude (i.e., $|h_{\text{sp}} - h_{\text{bu}}|$) of each design. Tables III

Accepted to Phys. Fluids 10.1063/5.0100100

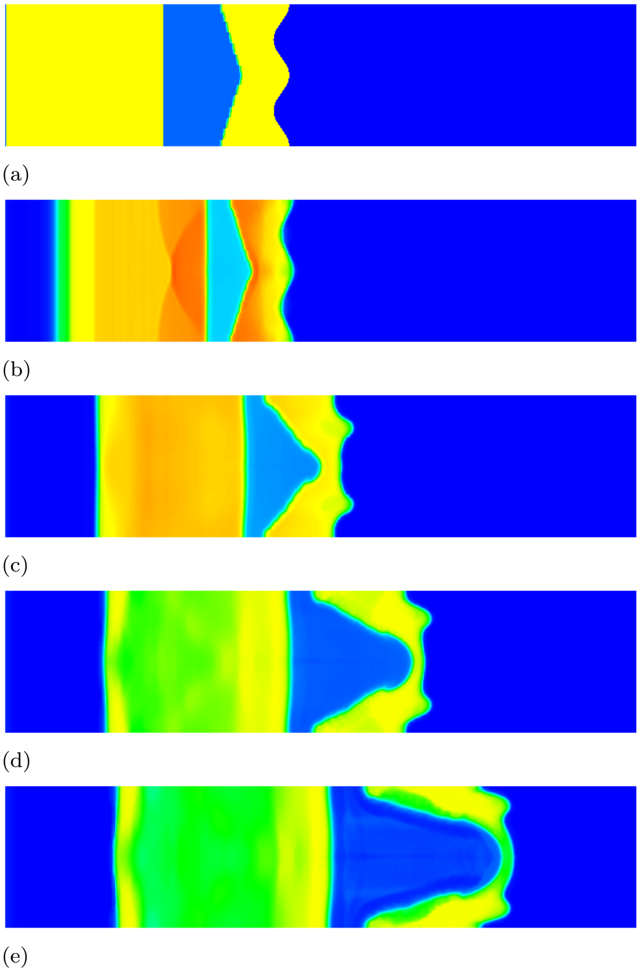
(a)
(b)
(c)
(d)
(e)

FIG. 10: Density plots at several time instants after the impactor strikes the target of an optimized design that uses a piecewise linear parameterization on the left-hand side of the target (allowing for a layer of lucite between impactor and copper target). This design largely suppresses any significant RMI spike growth and maintains a relatively flat interface on the right-hand side of the target (the side opposite to where the impactor strikes): (a) $\Delta t = 0.0$ μs (initial configuration at impact); (b) $\Delta t = 1.75$ μs; (c) $\Delta t = 3.50$ μs; (d) $\Delta t = 5.25$ μs; (e) $\Delta t = 7.0$ μs.

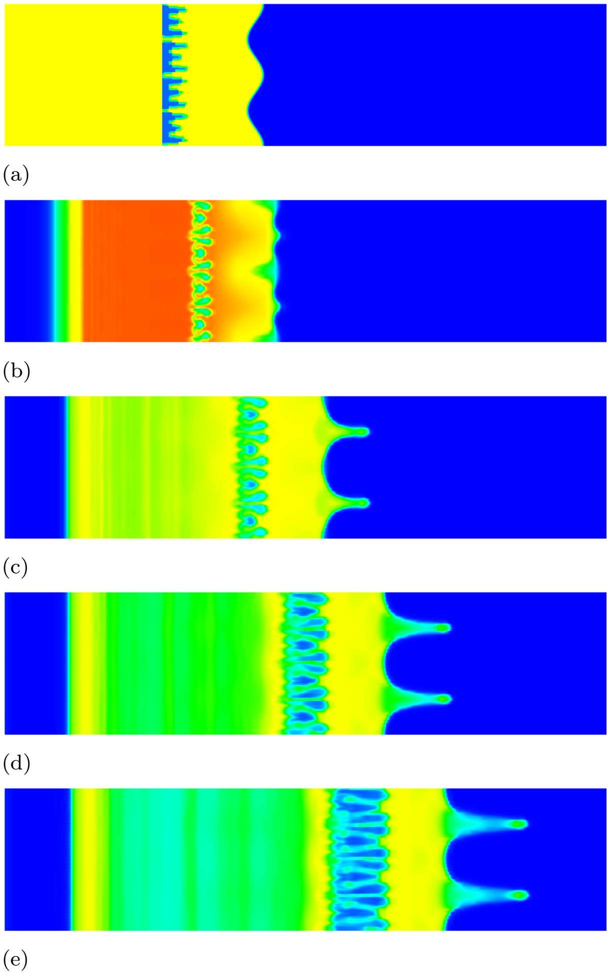
(a)
(b)
(c)
(d)
(e)

FIG. 11: Density plots at several time instants after the impactor strikes the target of an optimized design that uses the target compactness metric defined in Equation 6 as the objective function to be minimized. The PCHIP parameterization is used for the left-hand side of the target. This design partially suppresses RMI spike growth on the right-hand side of the target while simultaneously suppressing bubble growth on the left-hand side: (a) $\Delta t = 0.0$ μs (initial configuration at impact); (b) $\Delta t = 1.75$ μs; (c) $\Delta t = 3.50$ μs; (d) $\Delta t = 5.25$ μs; (e) $\Delta t = 7.0$ μs.

and IV show $|h_{\mathrm{sp}} - h_{\mathrm{bu}}|$ and the percent reduction for the designs in Figures 7–11 at 7 μs after impact occurs as well as at 4.5 μs after the phase inversion of the perturbations occurs. As is clear from Figure 12 and Tables III and IV, the optimized designs all significantly reduce the RMI spike growth below that of the baseline case in Figure 7 (i.e., Design 0 in Figure 12).

D. Discussion on design optimization results

The designs that result from our optimization process have several key features. The first key feature is the lucite that fills the cavities created by the optimized profile on the left-hand side of the target. This low-density lucite creates conditions that are similar to a RMI scenario where the Atwood number is positive (i.e., $\rho_1 < \rho_2$ and $A > 0$) and produces the rectifying RMI. For the rectifying RMI that we generate in our simulations, the Atwood number is equal to $A = 0.7657$ (where $\rho_1 = 1.186$ g/cm^3 for lucite and $\rho_2 = 8.938$ g/cm^3 for copper). In cases

Accepted to Phys. Fluids 10.1063/5.0100100

TABLE III: Comparison of the percent reduction in the average value of $|h_{\mathrm{sp}} - h_{\mathrm{bu}}|$ for the average of all tracer pairs for the designs in Figures 7–11 at 7 μs after the impact occurs and at 4.5 μs after the phase inversion of the perturbations occurs. The values in this table correspond to the tracer data in Figure 12(a).

	7 μs after impact		4.5 μs after inversion	
Design	$\|h_{\mathrm{sp}} - h_{\mathrm{bu}}\|$ [cm]	% Reduction	$\|h_{\mathrm{sp}} - h_{\mathrm{bu}}\|$ [cm]	% Reduction
0	0.6439	0.00%	0.5548	0.00%
1	0.0889	86.19%	0.0922	83.39%
2	0.1863	71.07%	0.1684	69.64%
3	0.1067	83.43%	0.1039	81.27%
4	0.5182	19.52%	0.4785	13.75%

TABLE IV: Comparison of the percent reduction in the average value of $|h_{\mathrm{sp}} - h_{\mathrm{bu}}|$ for the average of every other tracer pair for the designs in Figures 7–11 at 7 μs after the impact occurs and at 4.5 μs after the phase inversion of the perturbations occurs. The values in this table correspond to the tracer data in Figure 12(b).

	7 μs after impact		4.5 μs after inversion	
Design	$\|h_{\mathrm{sp}} - h_{\mathrm{bu}}\|$ [cm]	% Reduction	$\|h_{\mathrm{sp}} - h_{\mathrm{bu}}\|$ [cm]	% Reduction
0	0.6434	0.00%	0.5544	0.00%
1	0.0363	94.36%	0.0363	93.46%
2	0.0404	93.72%	0.0449	91.90%
3	0.0191	97.04%	0.0161	97.10%
4	0.5143	20.07%	0.4752	14.29%

where $A > 0$, a perturbation inversion does not occur as it does for the case where $A < 0$ (see diagrams in Figure 1)[26]. Instead, the protrusions created by the optimized profile on the left-hand side of the target begin to grow into the lower-density lucite. However, these protrusions have very little or no room to grow horizontally and almost immediately press up against the impactor. This causes the growing protrusions to immediately start rolling out or "mushrooming" [see Figure 13(b)]. Nevertheless, these protrusions continue to grow (possibly penetrating into the impactor) and this unstable growth puts stress on the target material. The lucite cavity region also has lower shock impedance Z than the copper target and creates the conditions necessary for compression waves to reverberate through the target and contributes to vorticity deposition that produces the rectifying RMI (we discuss this further in Section III E).

Another key feature of our optimized profiles is a sharp corner or indentation that protrudes into the target material on the left-hand side of the target. This sharp point acts as a stress concentration point (i.e., the stress in this region is higher than in the surrounding region in the target). In a standard RMI scenario, the stress created by the unstable spike growth leads to the formation of bubbles between the spikes. A stress concentration point between two rectifying RMI spikes (on the left-hand side of the target) appears to exacerbate the bubble effect, which creates a relatively large bubble that penetrates deep into the target as it develops [see Figure 13(b)]. This exacerbated RMI bubble has the effect of putting vertical stress on the perturbations on the right-hand side of the target. This vertical stress alters the direction of vorticity along the right-hand side of the target and redirects the velocity of the growing perturbations on the right-hand side of the target in a more vertical direction. This counteracts much of the RMI spike growth that would normally arise on the right-hand side of the target.

A third key feature is the difference in the number of periods between the optimized profile on the left-hand side of the target and the perturbations on the right-hand side of the target. As previously mentioned, we found that using half the number of periods on the left-hand side of the target (i.e., $N_l = N_r/2$) to be the most effective for suppressing spike growth on the right-hand side of the target. This is likely due to the pinching and flattening effect that the exacerbated bubbles from the rectifying RMI have on the right-hand side perturbations.

Accepted to Phys. Fluids 10.1063/5.0100100

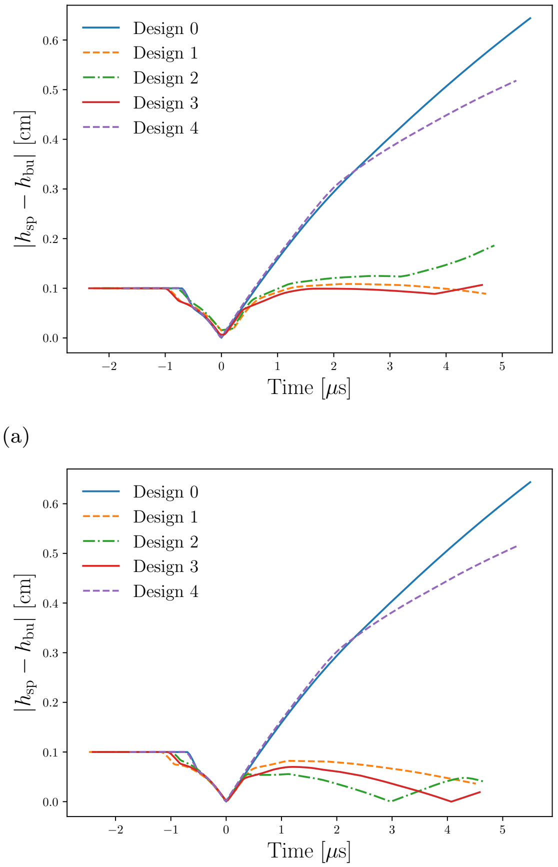

(a)

(b)

FIG. 12: Tracer plots for the designs shown in Figure 7 (Design 0, i.e., the baseline case), Figure 8 (Design 1), Figure 9 (Design 2), Figure 10 (Design 3), and Figure 11 (Design 4). The tracer data in these plots represents the amplitude difference between the spike and bubble tracer pairs (i.e., $|h_{\mathrm{sp}} - h_{\mathrm{bu}}|$). Note that the data in these plots has been shifted such that the phase inversion of the perturbations occurs at time $t = 0.0\ \mu s$: (a) Average of all tracer pairs [i.e., $i = 1, 2, 3, \dots, N_r$ in Equation (5)]; (b) Average of every other tracer pair (corresponding to where the most significant flattening of the right-hand side interface occurs) [i.e., $i = 1, 3, 5, \dots, N_r$ in Equation (6)].

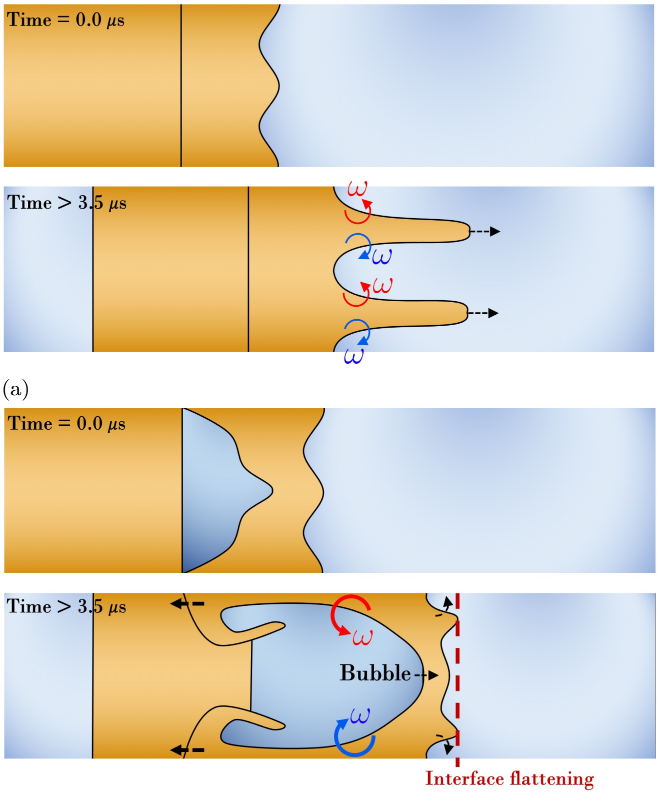

(a)

(b)

FIG. 13: These diagrams show the baseline case (no RMI suppression) in (a) and a general RMI suppression design in (b) at the initial time (i.e., $\Delta t = 0.0\ \mu$s) and at a later time (i.e., $\Delta t > 3.5\ \mu$s). For the design in (b), the positive Atwood number created on the left-hand side of the target by the optimized profile generates the rectifying RMI that includes a large bubble formation. This bubble formation contributes to suppressing RMI spike growth on the right-hand side of the target.

E. Shock-wave behvaior and vorticity analysis

The shock-wave behavior plays an important role in the vorticity deposition throughout the target and is necessary for fully understanding why our optimized profiles are effective at suppressing RMI spike growth. For the baseline case shown in Figure 7, the shock-wave behavior is relatively simple. When the impactor strikes the target, a normal shock wave is produced that moves to the right through the target. Once this shock wave reaches the air at the perturbed interface on the right-hand side of the target, the shock wave refracts and a rarefaction wave is produced that releases the pressure in the target. This rarefaction wave is produced because the low-density air has a much lower shock impedance Z than the copper target (see shock impedance discussion in Section II A). This results in vorticity deposition on only the right-hand side of the target, as seen in Figure 14, which shows the vorticity at several time instants for the baseline case. Note that red contours imply positive vorticity (counterclockwise) and blue contours imply negative vorticity (clockwise). As is clear from Figure 14(b) and (c), vorticity is high at the base of the growing RMI spikes and acts in opposite directions (clockwise and counterclockwise) on each half of these spikes. The balance of opposite direction vorticity for each spike is correlated to the growth of the spike in the horizontal direction. In Figure 14, there is essentially zero vorticity deposition on the left-hand side of the target, which is flat for the baseline case.

For the optimized design shown in Figure 9, the shock-

Accepted to Phys. Fluids 10.1063/5.0100100

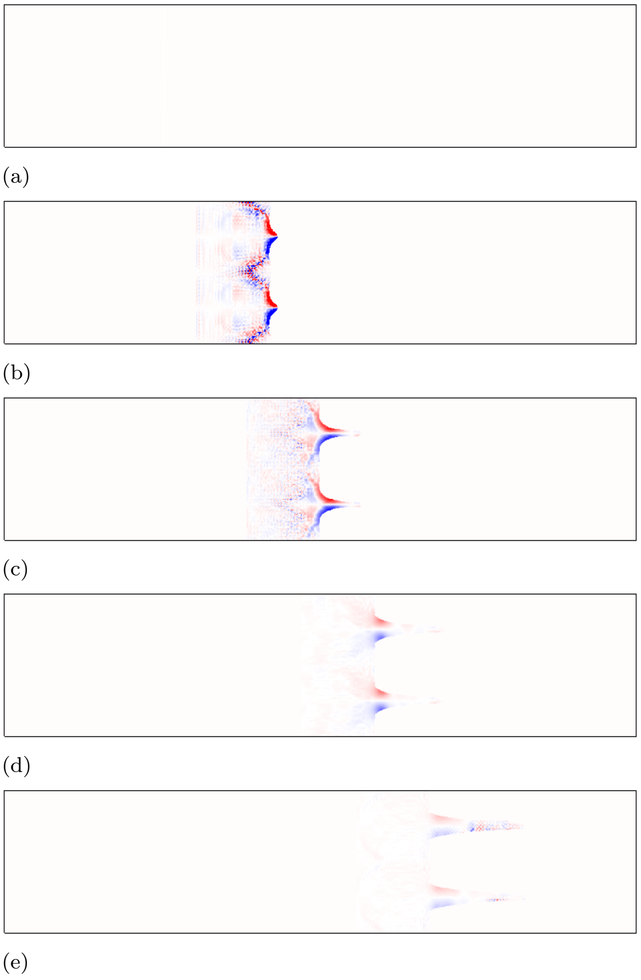

FIG. 14: Vorticity plots of the baseline case (no RMI suppression) shown in Figure 7 at several time instants. In these plots, the vorticity is capped at $\pm 0.5\ \mu\mathrm{s}^{-1}$ to more clearly show the contours at various times. Note that red contours imply positive vorticity (counterclockwise) and blue contours imply negative vorticity (clockwise): (a) $\Delta t = 0.0\ \mu s$ (initial configuration at impact); (b) $\Delta t = 1.75\ \mu s$; (c) $\Delta t = 3.50\ \mu s$; (d) $\Delta t = 5.25\ \mu s$; (e) $\Delta t = 7.0\ \mu s$.

wave behavior is slightly more complicated and the vorticity deposition on the left-hand side of the target is significant. Figure 15 shows a plot of pressure at several early time instants between $\Delta t = 0.75\ \mu s$ and $2.25\ \mu s$ for the design in Figure 9. When the impactor strikes the target, a normal shock wave is initially produced. However, the shock wave travels at higher velocity and at higher pressure through the copper (which has higher shock impedance Z than the lucite cavity region) [see Figure 15(a)]. The higher velocity portions of the shock wave move through the copper and lucite and eventually meet to produce a high-pressure region near the interface between the lucite cavity region and the copper target [see Figure 15(b)]. This high-pressure region reflects off this interface because lucite has a lower shock impedance Z than the copper target and reverberates radially outwards [see Figure 15(c)]. This radial compression wave then interacts with the corresponding wave from the adjacent periods to produce a high-pressure region within the copper protrusions [see Figure 15(d)]. Eventually, after significant vorticity deposition due to these reverberating shock waves, rarefaction waves release the pressure in the target.

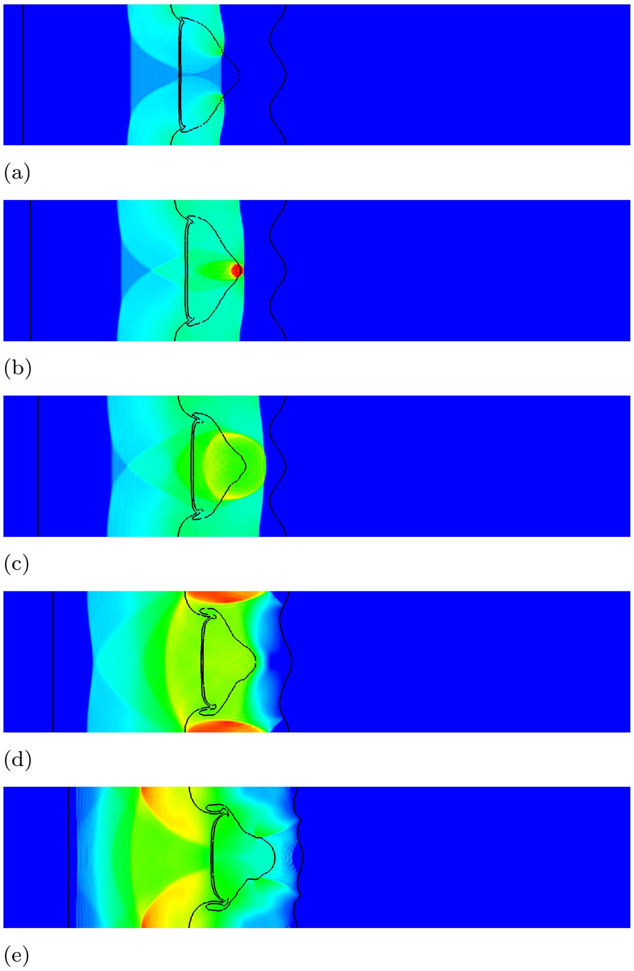

FIG. 15: Pressure plots of the optimized design shown in Figure 9 at several early time instants. In these plots, the pressure color mapping is bounded at 0 GPa (blue) and 70 GPa (red). The overlaid black lines represent the boundaries between materials (e.g., between the lucite cavity region and the copper target). These plots show the reverberating shock waves produced by the optimized profile. It is clear from (b) and (c) that a compression wave is partially reflected radially off the interface between the lucite cavity region and copper target: (a) $\Delta t = 0.75\ \mu s$; (b) $\Delta t = 1.00\ \mu s$; (c) $\Delta t = 1.25\ \mu s$; (d) $\Delta t = 1.75\ \mu s$; (e) $\Delta t = 2.25\ \mu s$.

This vorticity deposition produces the rectifying RMI on the left-hand side of the target. Figure 16 show the

Accepted to Phys. Fluids 10.1063/5.0100100

vorticity at several time instants for the optimized design in Figure 9. As the rectifying RMI is generated on the left-hand side of the target, the corresponding bubble penetrates deeply into the target and affects the vorticity on the right-hand side of the target. The result is that the balanced vorticity for each spike (which occurs in the baseline case) becomes unbalanced, causing the spikes on the right-hand side of the target to move more vertically and reducing growth in the horizontal direction. This creates the "pinching" effect seen in Figure 9(d) and (e) that contributes to the flattening of the right-hand side of the target.

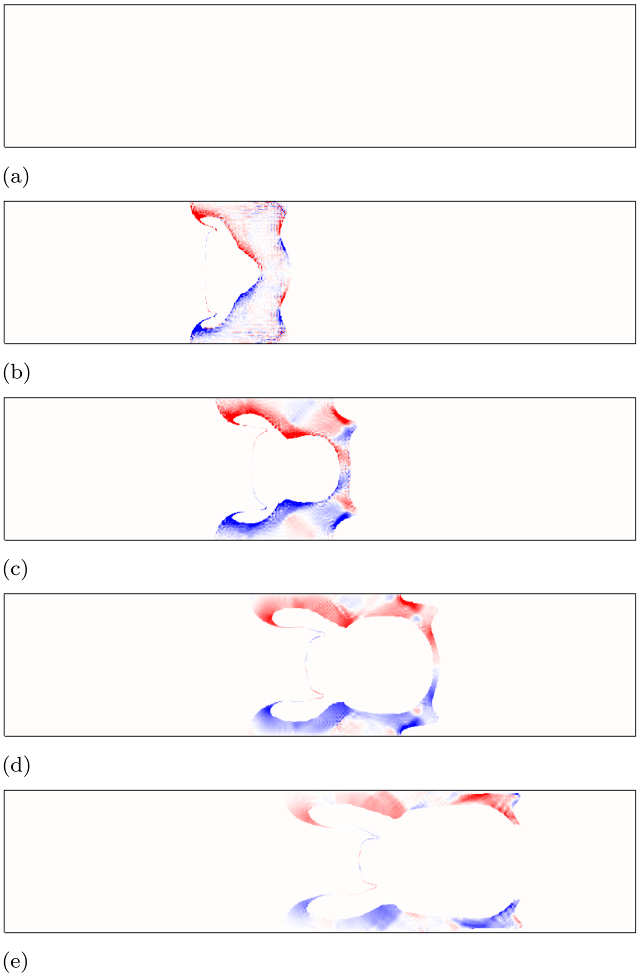

FIG. 16: Vorticity plots of the optimized design shown in Figure 9 at several time instants. In these plots, the vorticity is capped at ±0.5 μs^{-1} to more clearly show the contours at various times. Note that red contours imply positive vorticity (counterclockwise) and blue contours imply negative vorticity (clockwise): (a) $\Delta t = 0.0\ \mu s$ (initial configuration at impact); (b) $\Delta t = 1.75\ \mu s$; (c) $\Delta t = 3.50\ \mu s$; (d) $\Delta t = 5.25\ \mu s$; (e) $\Delta t = 7.0\ \mu s$.

IV. CONCLUSIONS

Our results show that it is possible to reduce and suppress RMI growth using gradient-free design optimization methods. Our optimized designs achieve suppression of RMI spike growth by using an optimized profile on the impactor side of the target (the side opposite to the initially perturbed interface) that generates a rectifying RMI. This rectifying RMI nearly completely counteracts RMI spike growth of the initially perturbed interface. In our analysis, we have identified several key features of our optimized designs that are necessary for suppressing RMI spike growth at the perturbed interface. These include several geometric and other features of the optimized profile that are particularly favorable for generating this rectifying RMI. We have also investigated shock-wave behavior and vorticity deposition for our optimized designs and found that the optimized profiles significantly increase vorticity deposition on the impactor side of the target by producing reverberating shock waves in the target. These reverberating shock waves play a significant role in instigating the rectifying RMI.

Overall, the methods that we have developed are very successful at suppressing RMI spike growth at an initially perturbed interface that has been impulsively accelerated using a shock wave. Future work will involve applying the design optimization methodologies that we have developed in this work to other RMI scenarios involving different materials, target geometries, and compression conditions. This may include a multi-objective optimization where the objective functions in Equations (5) and (6) are simultaneously minimized to reduce RMI spike growth while maintaining target compactness. Another area for future research may be to use design optimization to exacerbate RMI spike growth (rather than suppressing it as we have done in this work). Additionally, shock-compression experiments will be needed to further validate the results that we have presented in this study and possibly help guide future computational work.

ACKNOWLEDGMENTS

This work was performed under the auspices of the U.S. Department of Energy by Lawrence Livermore National Laboratory under Contract DE-AC52-07NA27344 and was supported by the LLNL-LDRD Program under Project No. 21-SI-006. We also thank Y. Choi, J. R. Gambino, A. B. Kostinski, R. N. Rieben, and W. J. Schill for helpful discussions and guidance related to the research presented in this paper.

DATA AVAILABILITY

The data that support the findings of this study are available from the corresponding author upon reasonable request.

Accepted to Phys. Fluids 10.1063/5.0100100

Appendix A: Material model validation

To demonstrate that our material equations of state and strength models are appropriate for the high-pressure regimes that we consider in this study, we compare simulation results obtained from the hydrodynamics code MARBL to an analytical scaling law developed by Dimonte et al.[13]. The Dimonte et al.[13] relation provides a correlation between the maximum amplitude of the RMI spike and the peak growth rate of the RMI spike. Under certain compression conditions, the RMI perturbation growth is halted due to the strength of the solid material at the interface (e.g., copper). This implies that there is a maximum spike amplitude $\max(h_{\text{sp}})$ that can be obtained for a given set of compression conditions. The plot in Figure 17(a) shows the spike amplitude h_{sp} versus time for our simulation setup using several different impactor velocities. As seen in this plot, the RMI spike growth is largely arrested after a certain period of time and the spike amplitude levels off to an approximately constant value[8,13]. The Dimonte et al.[13] analytical relation provides a means of predicting this maximum spike amplitude $\max(h_{\text{sp}})$ for a given set of material and compression conditions.

The Dimonte et al.[13] relation draws from the Piriz et al.[8] relation, which is derived by integrating the equation of motion for the linear evolution of the perturbed material interface. Piriz et al. assume that the material behaves as a Hookean solid (i.e., as a linearly elastic medium) below the yield criterion. These relations are also developed under the assumption that the upstream material through which the shock wave is initially moving can be approximated as behaving in an elastic–perfectly plastic manner (although we use the Steinberg–Guinan strength model[36] in our simulations) that follows the Prandtl–Reuss flow rule with the von Mises yield criterion[8]. According to Dimonte et al.[13], a RMI strength parameter h_Y can be written as a combination of other properties to obtain the following dimensionless form[13]

$$kh_Y = \frac{\rho_1}{Y}|\dot{h}^0_{\text{sp}}|^2 \tag{A1}$$

where k is the wave number of the interface perturbations, ρ_1 is the density of the upstream material (prior to shock loading), Y is the maximum yield stress of this material (we use $Y = 6.4 \times 10^{-3}$ Mbar for copper), and $\dot{h}^0_{\text{sp}}$ is the peak growth rate of the RMI spike, such that $\dot{h}^0_{\text{sp}} = \max(dh_{\text{sp}}/dt)$. The wave number k is defined as $k = 2\pi/\lambda$ where λ is the wavelength of the interface perturbations. The maximum spike amplitude h_{sp} can be written as a linear function of kh_Y as

$$kh_{\text{sp}} = \beta_0 + \beta_1 kh_Y \tag{A2}$$

where β_0 and β_1 are constants that are dependent on the system under consideration. Dimonte et al. found that $\beta_0 \approx 0.08$ and $\beta_1 \approx 0.24$ work well for scenarios where $A \approx -1$, such as the scenario that we consider in this work.

We use Equations (A1) and (A2) (setting $\beta_0 = 0.08$ and $\beta_1 = 0.24$) and compare this analytical relation with our numerical simulation. Figure 17(b) shows a comparison between the analytical relation of Equation (A2) and the maximum spike amplitude kh_{sp} for several simulation results. As is clear from the results in Figure 17(b), our simulations appear to be well approximated by the analytical relation of Equation (A2). Note that one caveat to the analytical relation of Equation (A2) is that it is only valid for kh_Y below a certain point. For values of kh_Y above this point, the RMI spikes grow quite rapidly and nonlinearly and the assumptions used to develop the relation in Equation (A2) tend to break down. This relation is also only strictly applicable when the strength model is approximated as being elastic–perfectly plastic. However, our simulations, which use the Steinberg–Guinan strength model for copper, appear to be well approximated by the Dimonte et al. relation.

Appendix B: Differential evolution optimization

Gradient-free optimization methods provide a relatively straight forward means of exploring the parameter space without requiring the gradient of the objective function. They are also capable of searching for a global minimum, whereas gradient-based methods are often restricted to finding local minima. There exists a vast variety of gradient-free methods and most employ a directed random search that attempts to balance exploration versus exploitation (also called diversification versus intensification). It is important to note that “No Free Lunch” theorems[38] show that most gradient-free methods perform as well on average as any other method. Therefore, we have not exhaustively investigated gradient-free methods, but have instead simply selected differential evolution optimization (DEO)[39,40], an evolutionary algorithm that shares some similarities with a genetic algorithm. Several studies in prior literature have found DEO to be useful for solving design optimization problems that also involve hydrodynamics simulations[41–43]. We use a variation of the DEO algorithm in the SciPy.optimize software package in our analysis[44]. A brief description of this algorithm is provided in the following paragraphs, but additional details on DEO can be found in the work of Storn and Price[39], the developers of this algorithm.

The first step of the DEO algorithm is to generate an initial set or population of trial parameter vectors using Latin hypercube sampling (LHS) to ensure that these values sufficiently span the parameter search space. We designate these trial parameter vectors as $\vec{x}_{i,G}$, where the subscript i is the index of a given trial vector within the population and G is the iteration or “generation” number. The elements of these parameter vectors correspond to the individual parameters of interest. The developers of the DEO algorithm recommend using a population size containing $5D$ to $10D$ parameter vectors, where D is the number of parameters used[39]. These trial parameter

Accepted to Phys. Fluids 10.1063/5.0100100

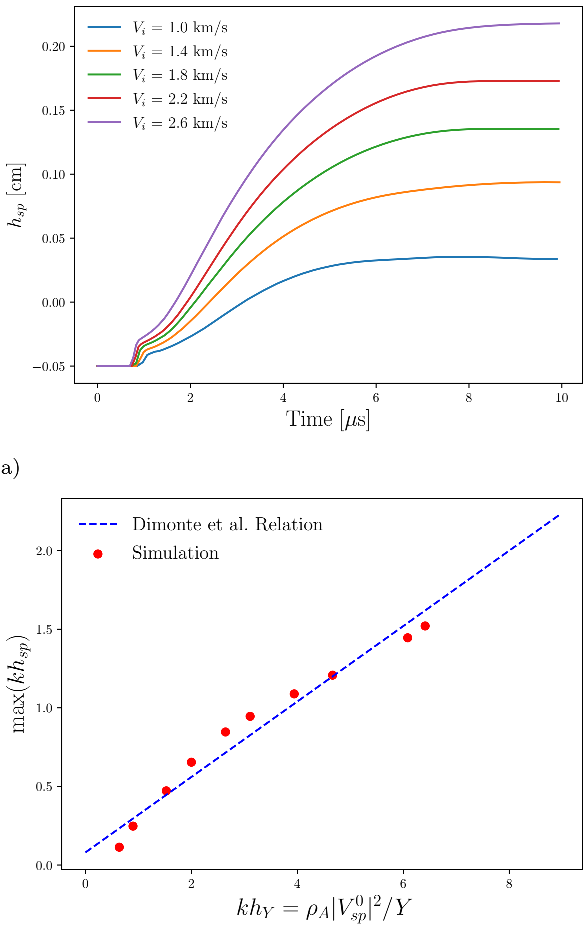

(a)

(b)

FIG. 17: The relation of Dimonte et al.[13] provides a means for partially validating the material models used in our simulations. The relation was developed using an elastic–perfectly plastic strength model for copper, but matches our simulation results well (which use the Steinberg–Guinan strength model): (a) RMI spike amplitude h_{sp} versus time for our simulations that involve a range of impactor velocities V_i. As seen in the plot, the spike growth is eventually arrested and settles to an approximately constant value; (b) A comparison of the Dimonte et al. relation with the results from several of our simulations at various impactor velocities.

vectors $\vec{x}_{i,G}$ are then individually substituted into hydrodynamics simulations as described in Section II B, which can all be run in parallel for the entire population of trial parameter vectors for a given generation of the DEO algorithm. These hydrodynamics simulations output data for computing the objective function (e.g., tracer data for the amplitude of the spike h_{sp} and bubble h_{bu} for each period of the perturbed interface). This data is then substituted into the objective function of Equation (5) or (6) to determine the relative fitness of each trial parameter vector for reducing RMI spike growth.

The trial parameter vector that minimizes the objective function the most is selected from amongst the population of vectors. We refer to this parameter vector as the "best" parameter vector $\vec{x}_{best,G}$ and this vector is used in the next generation of the DEO algorithm to produce a set of "mutant" vectors in the following way. Two parameter vectors are individually selected at random from the population of the previous generation. These two parameter vectors (which we designate as $\vec{x}_{r_1,G}$ and $\vec{x}_{r_2,G}$) are subtracted to produce a differential variation[39], which is scaled by a weighting factor F. The scaled differential variation is then added to the best parameter vector to produce a mutant vector as shown in the following equation:

$$\vec{v}_{i,G+1} = \vec{x}_{best,G} + F \cdot (\vec{x}_{r_1,G} - \vec{x}_{r_2,G}). \tag{B1}$$

This is repeated until a full population of mutant vectors for the next generation $\vec{v}_{i,G+1}$ is produced.

After generating the mutant vectors, each trial parameter vector in the previous generation population undergoes a round of "crossover" with the mutant vectors. For the crossover process, we refer to the trial parameter vectors of the previous generation $\vec{x}_{i,G}$ as the target vectors. For each element in a target vector, a random number rand(j) between 0 and 1 is chosen. If this random number is less than or equal to the crossover probability CR, then the parameter value from the mutant vector is used in the trial vector for the next generation $\vec{x}_{i,G+1}$. Otherwise, the parameter value for the trial vector remains the same as the value from the previous generation. The crossover process for a single vector element $x_{ji,G+1}$ can be represented as

$$x_{ji,G+1} = \begin{cases} v_{ji,G+1}, & \text{if } [\text{rand}(j) \leq CR] \\ x_{ji,G}, & \text{if } [\text{rand}(j) > CR] \end{cases} \tag{B2}$$
$$j = 1, 2, \ldots, D.$$

where the subscript j is the index of a given element within the parameter vector. An illustration of the crossover process is also provided in Figure (18). Note that the choice of the weighting factor F and the crossover probability CR are generally application specific. For our application, we set $F = 0.5$ and $CR = 0.75$.

This new set of trial parameter vectors $\vec{x}_{i,G+1}$ is then used as the trial population for the next generation of the DEO algorithm and are individually substituted into hydrodynamics simulations. The hydrodynamics data is again used to find the best parameter vector $\vec{x}_{best,G}$ for the current generation using the objective function of Equation (5). This process is iteratively repeated until a stopping criterion is reached. This stopping criterion can be specified as a specific number of generations or as a convergence criterion such as

$$\frac{\sigma_{\phi_i}}{\langle \phi_i \rangle} < \epsilon, \tag{B3}$$

Accepted to Phys. Fluids 10.1063/5.0100100

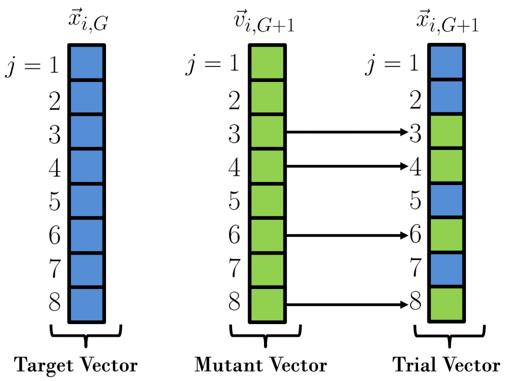

FIG. 18: For each generation of the DEO algorithm, a population of mutant vectors $\vec{v}_{i,G+1}$ is produced using the relation in Equation (B1). After creating a population of mutant vectors $\vec{v}_{i,G+1}$, these mutant vectors undergo a round of crossover with the target vectors $\vec{x}_{i,G}$ (i.e., the trial vectors of the previous generation G) to produce a new set of trial vectors for the next generation $\vec{x}_{i,G+1}$. To perform this crossover process, a random number between 0 and 1 is selected for each vector element j. If this random number is less than or equal to the crossover probability CR, the corresponding element from the mutant vector $\vec{v}_{i,G+1}$ is used to produce $\vec{x}_{i,G+1}$. Otherwise, the element from the previous trial vector $\vec{x}_{i,G}$ is used. This crossover selection process is described by Equation (B2). Reproduced from D. M. Sterbentz et al., J. Appl. Phys. 128, 195903 (2020), with the permission of AIP Publishing.

where σ_{ϕ_i} is the standard deviation of the objective function across all parameter vectors of the current generation, $\langle \phi_i \rangle$ is the average value of the objective function across all parameter vectors, and ϵ is a specified convergence tolerance that we set equal to $\epsilon = 0.01$. Once the stopping criterion is reached, the best parameter vector for the current generation is output and ideally contains the optimal set of parameters for minimizing the objective function. This constitutes the DEO algorithm that we apply to the RMI reduction design problem.

[1] J. Kane, R. Drake, B. Remington, An evaluation of the Richtmyer–Meshkov instability in supernova remnant formation, Astrophys. J. 511 (1) (1999) 335.

[2] D. Arnett, The role of mixing in astrophysics, Astrophys. J. Suppl. Ser. 127 (2) (2000) 213.

[3] J. D. Lindl, R. L. McCrory, E. M. Campbell, Progress toward ignition and burn propagation in inertial confinement fusion, Phys. Today 45 (9) (1992) 32.

[4] J. H. Hammer, M. Tabak, S. C. Wilks, J. D. Lindl, D. S. Bailey, P. W. Rambo, A. Toor, G. B. Zimmerman, J. L. Porter Jr, High yield inertial confinement fusion target design for a z-pinch-driven hohlraum, Phys. Plasmas 6 (5) (1999) 2129–2136.

[5] Y. Aglitskiy, A. Velikovich, M. Karasik, N. Metzler, S. Zalesak, A. Schmitt, L. Phillips, J. Gardner, V. Serlin, J. Weaver, et al., Basic hydrodynamics of Richtmyer–Meshkov-type growth and oscillations in the inertial confinement fusion-relevant conditions, Philos. Trans. R. Soc. A 368 (1916) (2010) 1739–1768.

[6] R. Betti, O. Hurricane, Inertial-confinement fusion with lasers, Nat. Phys. 12 (5) (2016) 435–448.

[7] A. Zylstra, O. Hurricane, D. Callahan, A. Kritcher, J. Ralph, H. Robey, J. Ross, C. Young, K. Baker, D. Casey, et al., Burning plasma achieved in inertial fusion, Nature 601 (7894) (2022) 542–548.

[8] A. R. Piriz, J. L. Cela, N. A. Tahir, D. H. Hoffmann, Richtmyer–Meshkov instability in elastic-plastic media, Phys. Rev. E 78 (5) (2008) 056401.

[9] W. Buttler, D. Oró, D. Preston, K. O. Mikaelian, F. Cherne, R. Hixson, F. Mariam, C. Morris, J. Stone, G. Terrones, et al., Unstable Richtmyer–Meshkov growth of solid and liquid metals in vacuum, J. Fluid Mech. 703 (2012) 60.

[10] B. J. Jensen, F. J. Cherne, M. B. Prime, K. Fezzaa, A. J. Iverson, C. Carlson, J. Yeager, K. J. Ramos, D. E. Hooks, J. C. Cooley, et al., Jet formation in cerium metal to examine material strength, J. Appl. Phys. 118 (19) (2015) 195903.

[11] Z. Sternberger, B. Maddox, Y. Opachich, C. Wehrenberg, R. Kraus, B. Remington, G. Randall, M. Farrell, G. Ravichandran, A comparative study of Rayleigh–Taylor and Richtmyer–Meshkov instabilities in 2D and 3D in tantalum, in: AIP Conf. Proc., Vol. 1793, AIP Publishing LLC, 2017, p. 110006.

[12] Z. Sternberger, Y. Opachich, C. Wehrenberg, R. Kraus, B. Remington, N. Alexander, G. Randall, M. Farrell, G. Ravichandran, Investigation of hydrodynamic instability growth in copper, Int. J. Mech. Sci. 149 (2018) 475–480.

[13] G. Dimonte, G. Terrones, F. J. Cherne, T. C. Germann, V. Dupont, K. Kadau, W. T. Buttler, D. M. Oro, C. Morris, D. L. Preston, Use of the Richtmyer–Meshkov instability to infer yield stress at high-energy densities, Phys. Rev. Lett. 107 (26) (2011) 264502.

[14] Q. Chen, L. Li, Y. Zhang, B. Tian, Effects of the atwood number on the Richtmyer–Meshkov instability in elastic-plastic media, Phys. Rev. E 99 (5) (2019) 053102.

[15] R. Samtaney, Suppression of the Richtmyer–Meshkov instability in the presence of a magnetic field, Phys. Fluids 15 (8) (2003) L53–L56.

[16] V. Wheatley, D. Pullin, R. Samtaney, Stability of an impulsively accelerated density interface in magnetohydrodynamics, Phys. Rev. Lett. 95 (12) (2005) 125002.

[17] T. Sano, T. Inoue, K. Nishihara, Critical magnetic field strength for suppression of the Richtmyer–Meshkov instability in plasmas, Phys. Rev. Lett. 111 (20) (2013) 205001.

[18] T. Sano, K. Ishigure, F. Cobos-Campos, Suppression of the Richtmyer–Meshkov instability due to a density transition layer at the interface, Phys. Rev. E 102 (1) (2020) 013203.

[19] M. Henry de Frahan, P. Movahed, E. Johnsen, Numerical simulations of a shock interacting with successive interfaces using the discontinuous Galerkin method: the multilayered Richtmyer–Meshkov and Rayleigh–Taylor instabilities, Shock Waves 25 (4) (2015) 329–345.

[20] L. Feng, J. Xu, Z. Zhai, X. Luo, Evolution of shock-accelerated double-layer gas cylinder, Phys. Fluids 33 (8) (2021) 086105.

[21] Y. Liang, X. Luo, On shock-induced heavy-fluid-layer evolution, J. Fluid Mech. 920.

[22] Y. Liang, X. Luo, Shock-induced dual-layer evolution, J. Fluid Mech. 929.

[23] Y. Liang, The phase effect on the Richtmyer–Meshkov instability of a fluid layer, Phys. Fluids 34 (3) (2022) 034106.

[24] B. Mohammadi, O. Pironneau, Shape optimization in fluid mechanics, Annu. Rev. Fluid Mech. 36 (2004) 255–279.

[25] N. J. Zabusky, Vortex paradigm for accelerated inhomogeneous flows: Visiometrics for the Rayleigh–Taylor and Richtmyer–Meshkov environments, Annu. Rev. Fluid Mech. 31 (1) (1999) 495–536.

[26] M. Brouillette, The Richtmyer–Meshkov instability, Annu. Rev. Fluid Mech. 34 (1) (2002) 445–468.

[27] W. Nellis, A. Mitchell, D. Young, Equation-of-state measurements for aluminum, copper, and tantalum in the pressure range 80–440 GPa (0.8–4.4 Mbar), J. Appl. Phys. 93 (1) (2003) 304–

Accepted to Phys. Fluids 10.1063/5.0100100

310.

[28] M. Armstrong, J. Nguyen, S. Aubry, W. Schill, J. Belof, H. Lorenzana, Use of shock wavefront curvature to modulate RMI jet growth, Bull. Am. Phys. Soc., 2022.

[29] J. Nguyen, S. Aubry, M. Armstrong, A. Hoff, J. Belof, H. Lorenzana, M. Staska, B. LaLone, Modulation of Richtmyer–Meshkov instability in gas gun experiments, Bull. Am. Phys. Soc., 2022.

[30] R. Anderson, A. Black, B. Blakeley, R. Bleile, J.-S. Camier, J. Ciurej, A. Cook, V. Dobrev, N. Elliott, J. Grondalski, C. Harrison, R. Hornung, T. Kolev, M. Legendre, W. Liu, W. Nissen, B. Olson, M. Osawe, G. Papadimitriou, O. Pearce, R. Pember, A. Skinner, D. Stevens, T. Stitt, L. Taylor, V. Tomov, R. Rieben, A. Vargas, K. Weiss, D. White, L. Busby, The multiphysics on advanced platforms project, Tech. Rep. Tech. rep., LLNL-TR-815869, Lawrence Livermore National Laboratory, Livermore, CA (United States) (2020). `doi:10.2172/1724326`.

[31] R. Rieben, Poster: The MARBL multi-physics code, in: Exascale Computing Project Annual Meeting, 2020. `doi:10.13140/RG.2.2.12326.14403`.

[32] R. W. Anderson, V. A. Dobrev, T. V. Kolev, R. N. Rieben, V. Z. Tomov, High-order multi-material ALE hydrodynamics, SIAM J. Sci. Comput. 40 (1) (2018) B32–B58.

[33] D. A. Young, Phase diagrams of the elements, University of California Press, 1991.

[34] R. More, K. Warren, D. Young, G. Zimmerman, A new quotidian equation of state (QEOS) for hot dense matter, Phys. Fluids 31 (10) (1988) 3059–3078. `doi:10.1063/1.866963`.

[35] D. A. Young, E. M. Corey, A new global equation of state model for hot, dense matter, J. Appl. Phys. 78 (6) (1995) 3748–3755. `doi:10.1063/1.359955`.

[36] D. Steinberg, S. Cochran, M. Guinan, A constitutive model for metals applicable at high-strain rate, J. Appl. Phys. 51 (3) (1980) 1498–1504.

[37] F. N. Fritsch, R. E. Carlson, Monotone piecewise cubic interpolation, SIAM J. Numer. Anal. 17 (2) (1980) 238–246. `doi:10.1137/0717021`.

[38] D. H. Wolpert, W. G. Macready, No free lunch theorems for optimization, IEEE Trans. Evol. Comp. 1 (1) (1997) 67–82.

[39] R. Storn, K. Price, Differential evolution–a simple and efficient heuristic for global optimization over continuous spaces, J. Glob. Optim. 11 (4) (1997) 341–359. `doi:10.1023/A:1008202821328`.

[40] K. Price, R. M. Storn, J. A. Lampinen, Differential evolution: A practical approach to global optimization, Springer Science & Business Media, 2006.

[41] J. R. Gambino, C. M. Tarver, H. K. Springer, Numerical parameter optimizations of the ignition and growth model for a HMX plastic bonded explosive, J. Appl. Phys. 124 (19) (2018) 195901. `doi:10.1063/1.5052339`.

[42] A. Nichols, J. Gambino, Toward a morphology aware detonation model, Tech. rep., Lawrence Livermore National Laboratory, Livermore, CA (United States) (2018).

[43] D. M. Sterbentz, J. R. Gambino, P. C. Myint, J.-P. Delplanque, H. K. Springer, M. C. Marshall, J. L. Belof, Drive-pressure optimization in ramp-wave compression experiments through differential evolution, J. Appl. Phys. 128 (19) (2020) 195903. `doi:10.1063/5.0023361`.

[44] P. Virtanen, R. Gommers, T. E. Oliphant, M. Haberland, T. Reddy, D. Cournapeau, E. Burovski, P. Peterson, W. Weckesser, J. Bright, S. J. van der Walt, M. Brett, J. Wilson, K. J. Millman, N. Mayorov, A. R. J. Nelson, E. Jones, R. Kern, E. Larson, C. J. Carey, İ. Polat, Y. Feng, E. W. Moore, J. VanderPlas, D. Laxalde, J. Perktold, R. Cimrman, I. Henriksen, E. A. Quintero, C. R. Harris, A. M. Archibald, A. H. Ribeiro, F. Pedregosa, P. van Mulbregt, SciPy 1.0 Contributors, SciPy 1.0: Fundamental Algorithms for Scientific Computing in Python, Nat. Methods 17 (2020) 261–272. `doi:10.1038/s41592-019-0686-2`.

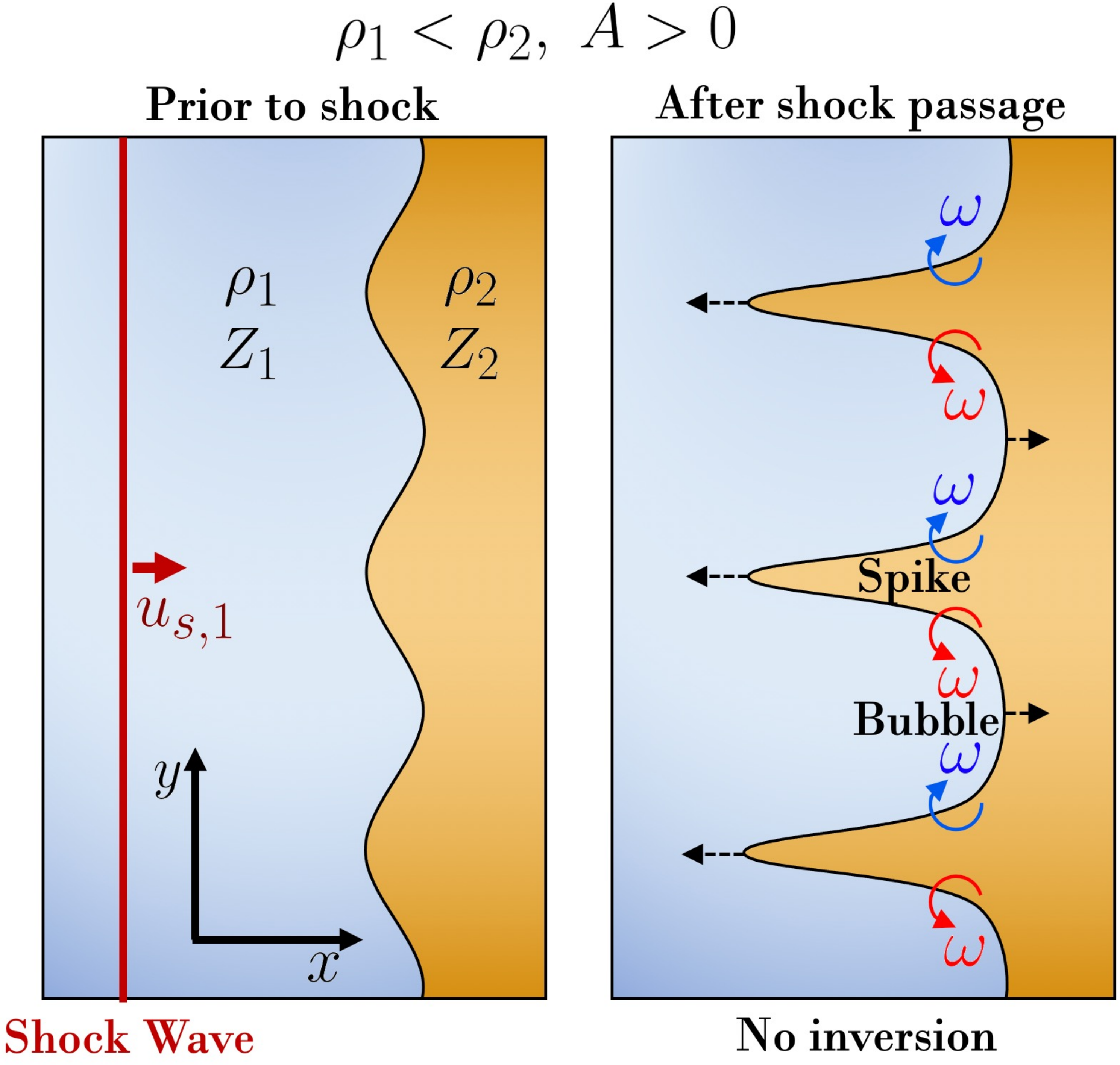
$\rho_1 < \rho_2,\ A > 0$
Prior to shock
After shock passage
ρ_1
Z_1
ρ_2
Z_2
$u_{s,1}$
y
x
ω
Spike
Bubble
Shock Wave
No inversion

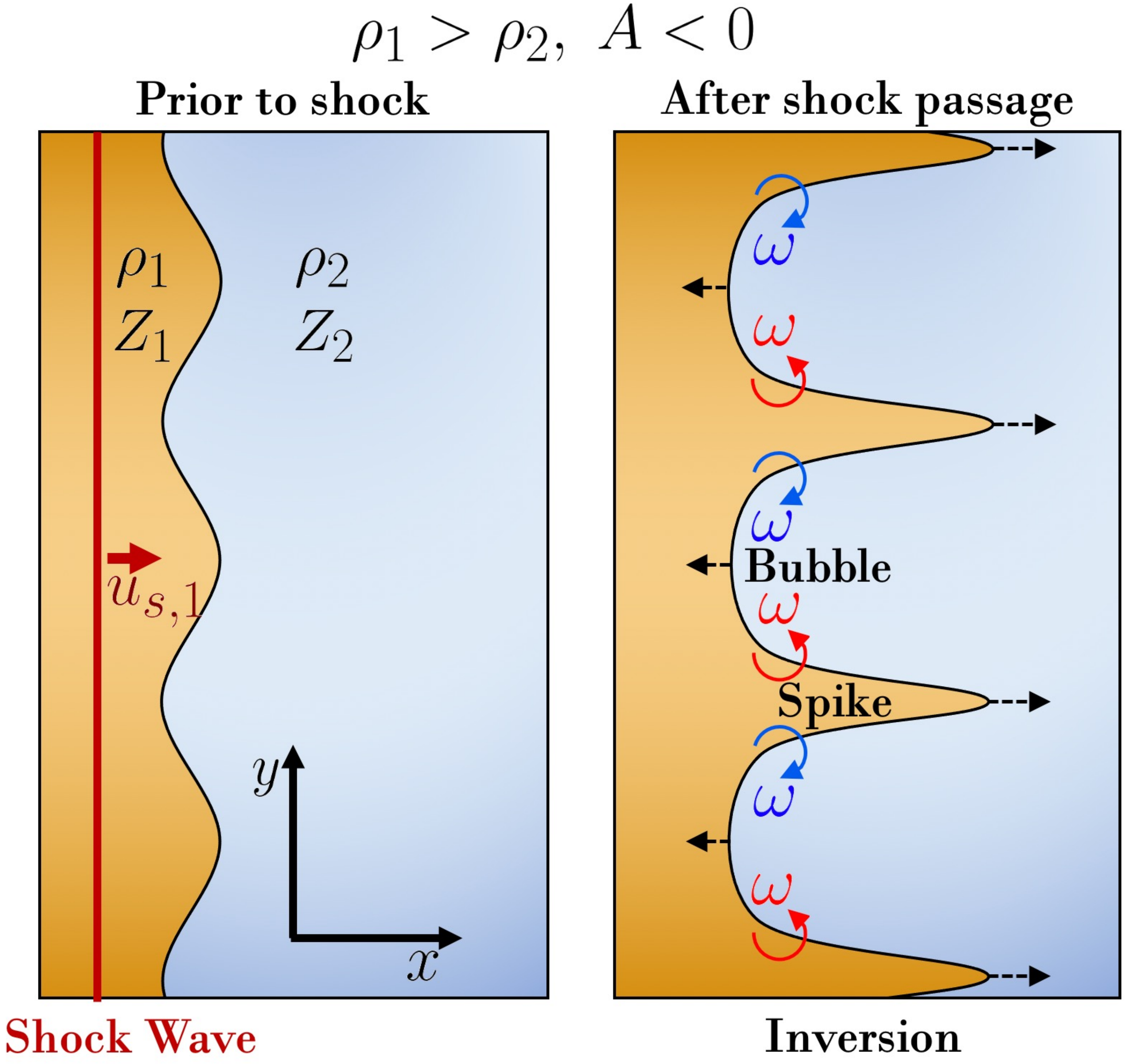
$\rho_1 > \rho_2,\ A < 0$
Prior to shock
After shock passage
ρ_1
Z_1
ρ_2
Z_2
$u_{s,1}$
y
x
Shock Wave
ω
Bubble
Spike
Inversion

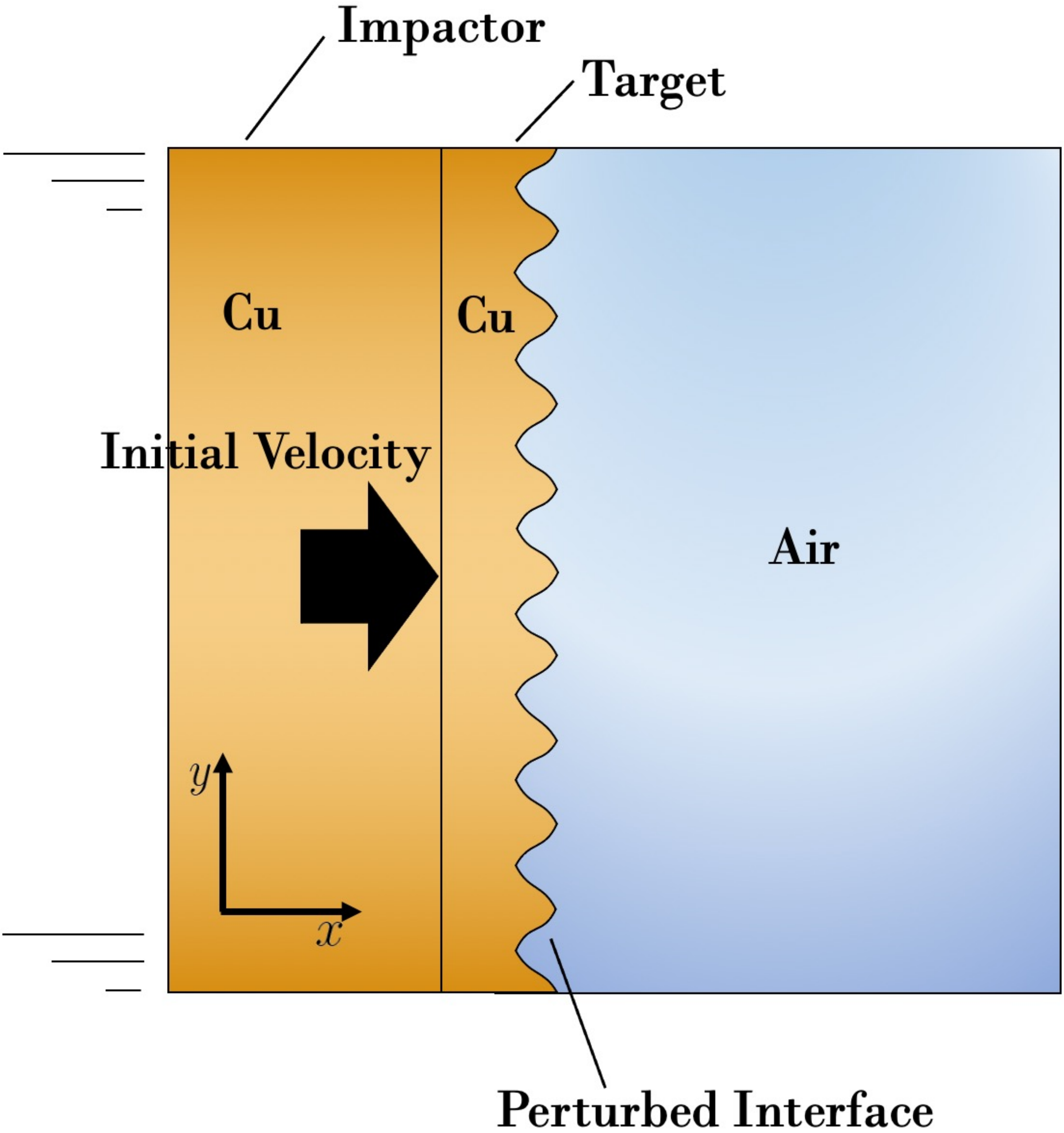
Impactor
Target
Cu
Cu
Initial Velocity
Air
y
x
Perturbed Interface

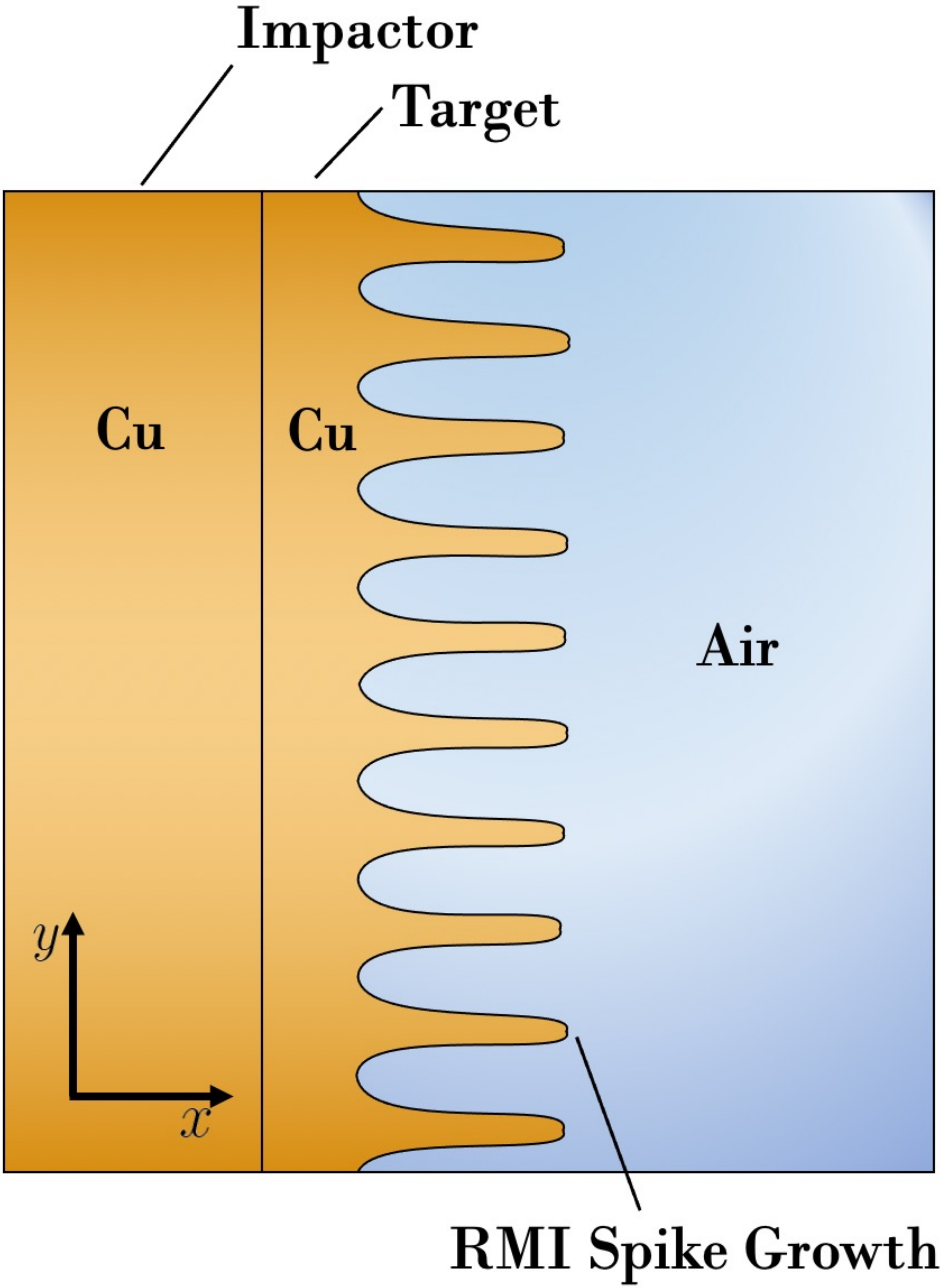
Impactor
Target
Cu
Cu
Air
y
x
RMI Spike Growth

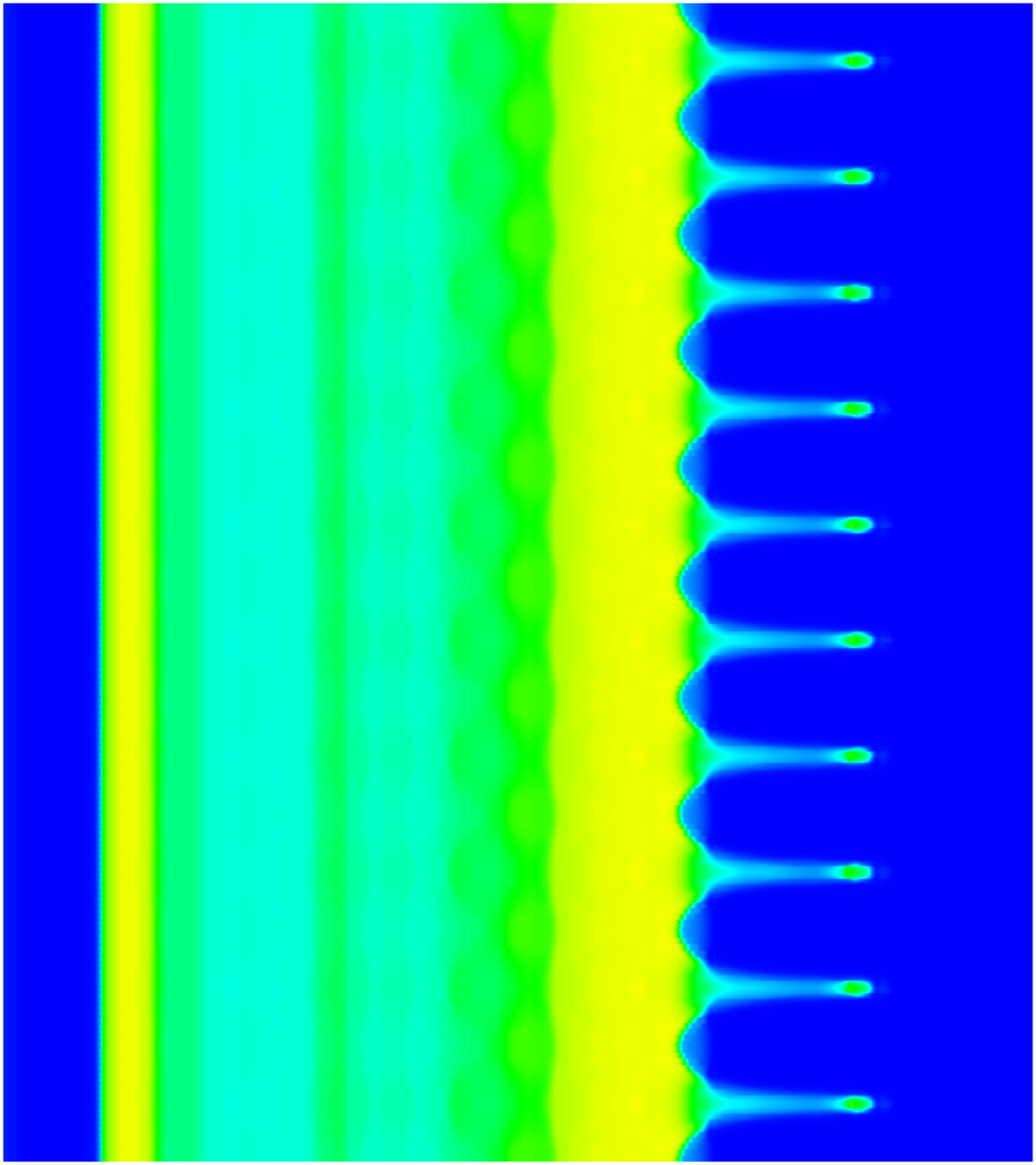

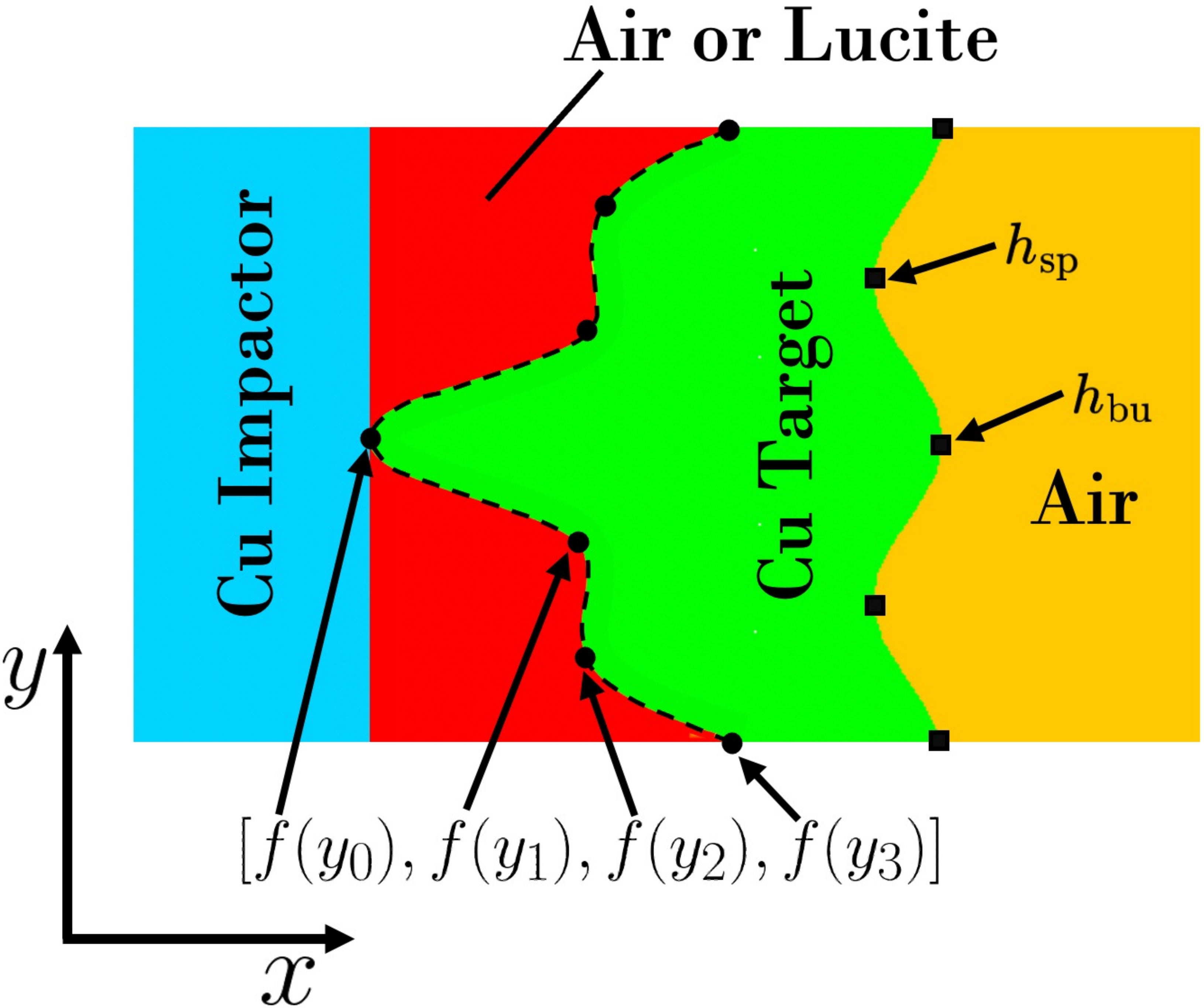
Air or Lucite
Cu Impactor
Cu Target
h_{sp}
h_{bu}
Air
$[f(y_0), f(y_1), f(y_2), f(y_3)]$
y
x

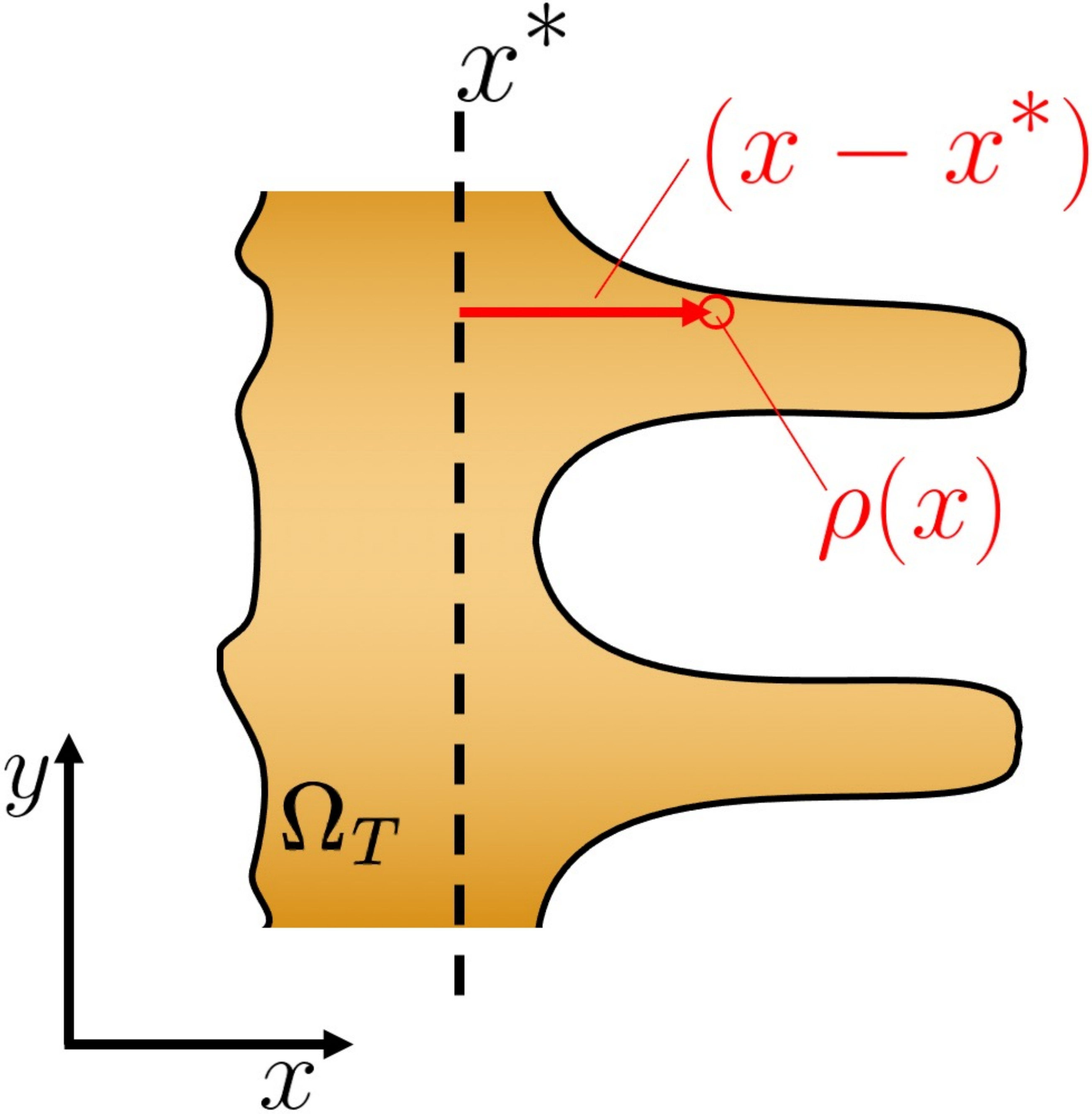
x^*
$(x - x^*)$
$\rho(x)$
Ω_T
y
x

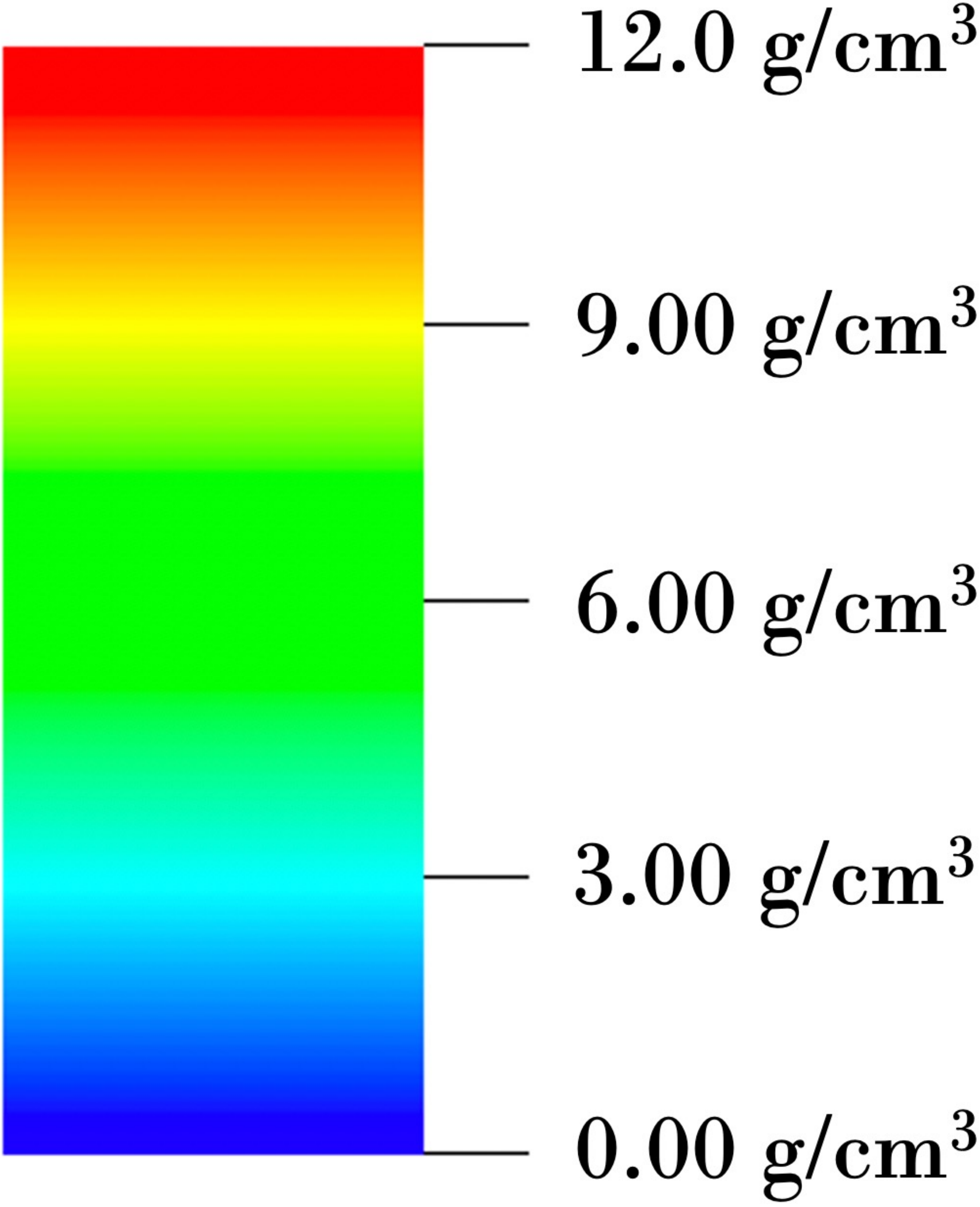
12.0 g/cm³
9.00 g/cm³
6.00 g/cm³
3.00 g/cm³
0.00 g/cm³

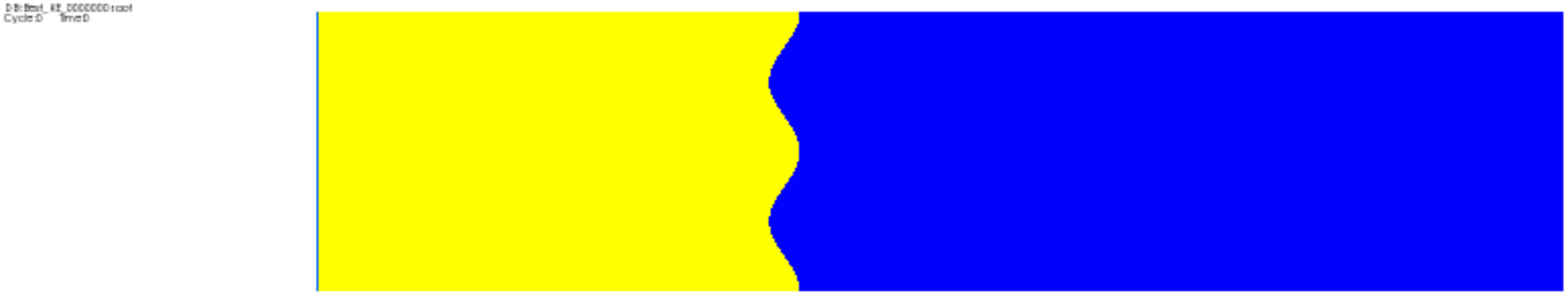
DB: Best_KE_00000000.root
Cycle: 0 Time:0

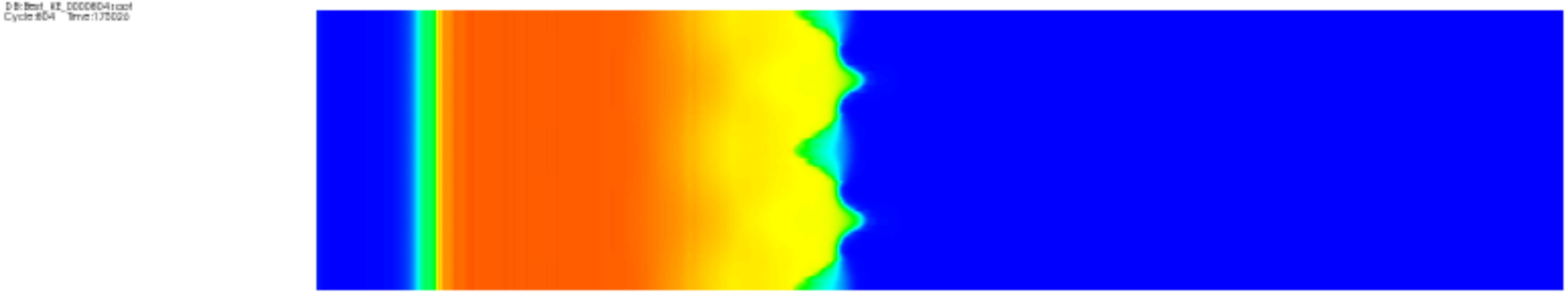
DB: Best_KE_0000804.root
Cycle:804 Time:175026

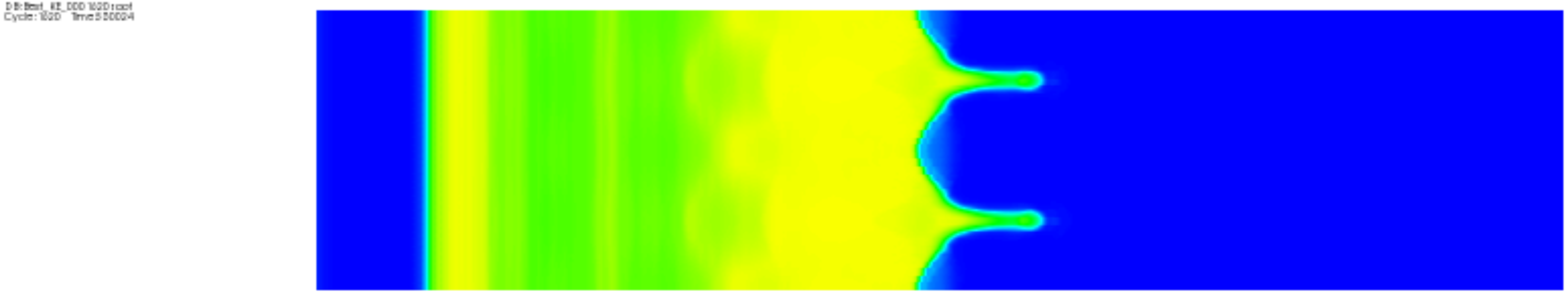
DB: Best_KE_000 1020.root
Cycle: 1020 Time:5.00024

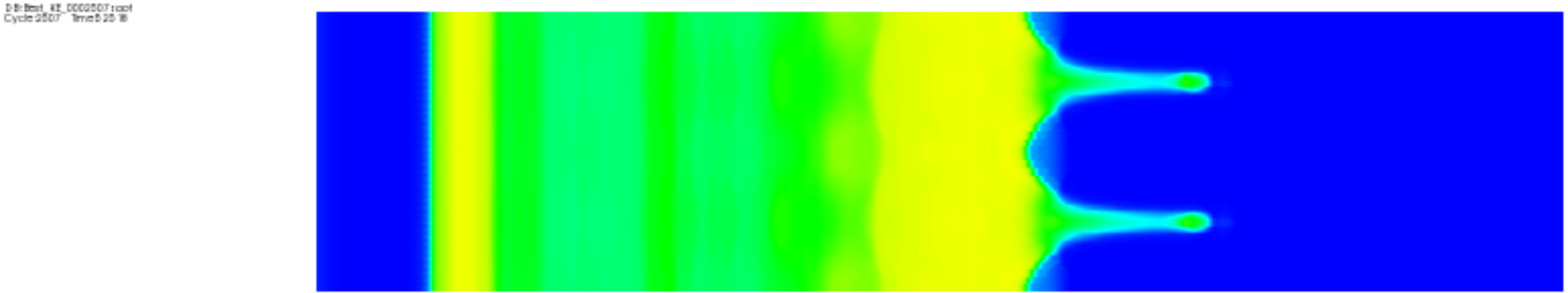
DB: Best_KE_0002507.root
Cycle:2507 Time:5.2516

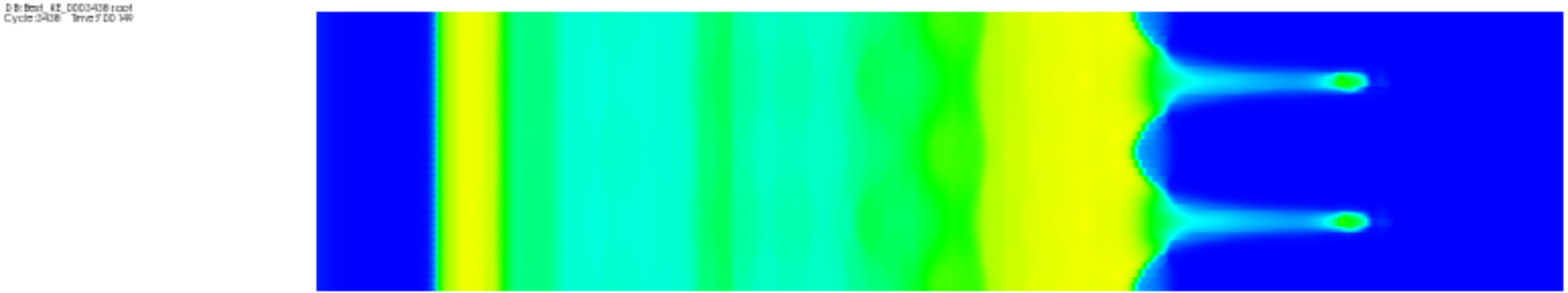
DB: Best_KE_00003408.root
Cycle: 3408 Time: 5.00149

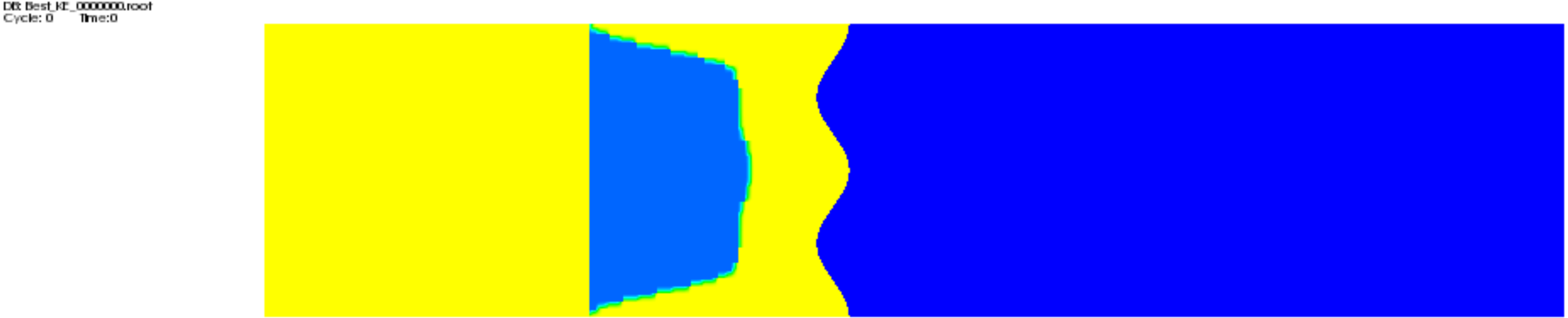
DB: Best_KE_0000000.root
Cycle: 0 Time:0

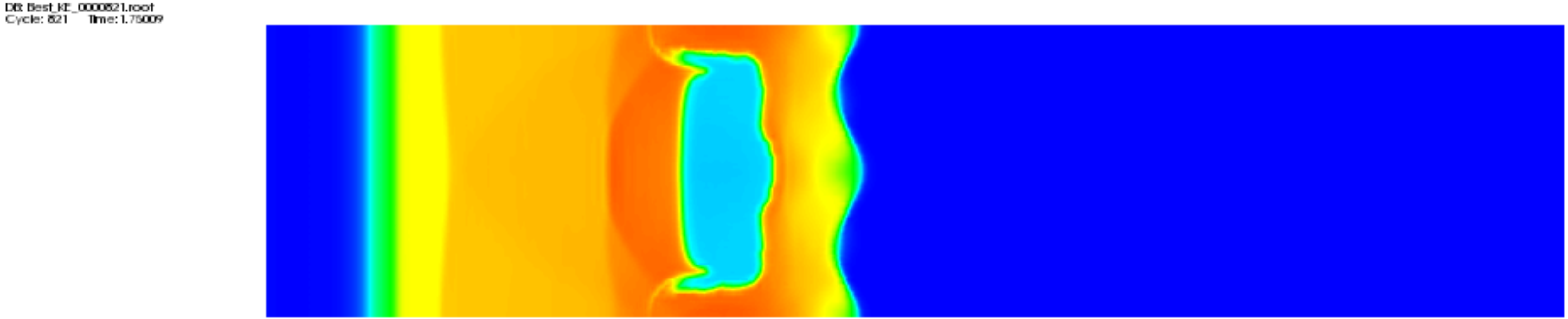
DB: Best_KE_0000821.root
Cycle: 821 Time: 1.75009

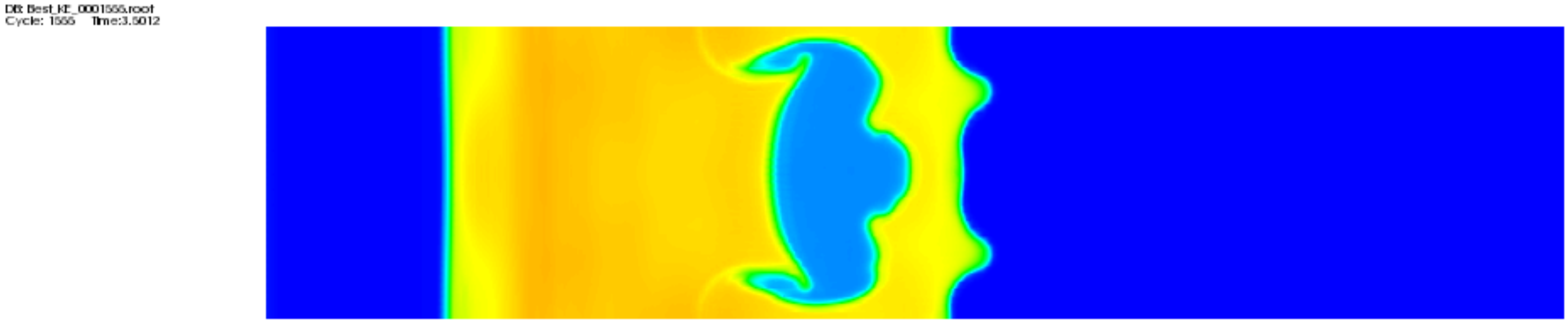
DB: Best_KE_0001555.root
Cycle: 1555 Time:3.5012

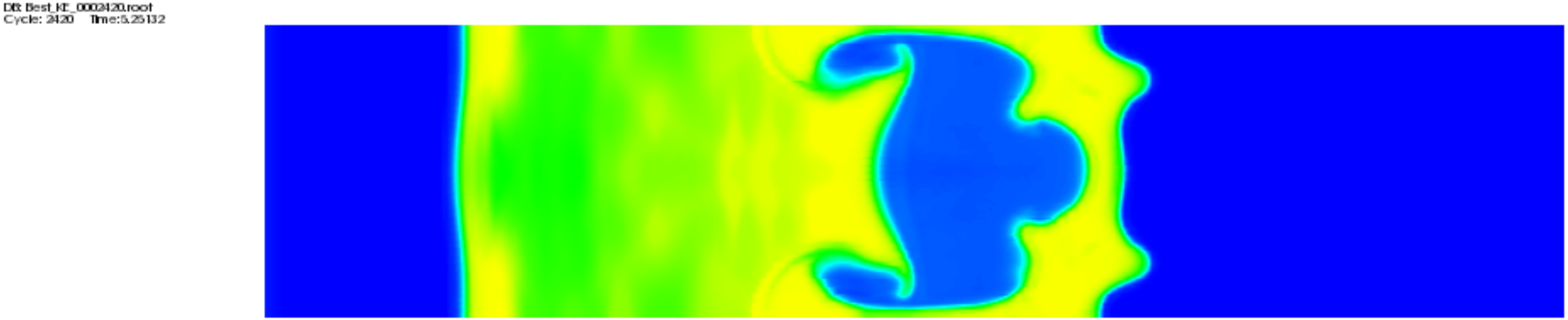
DB: Best_KE_0002420.root
Cycle: 2420 Time:5.25132

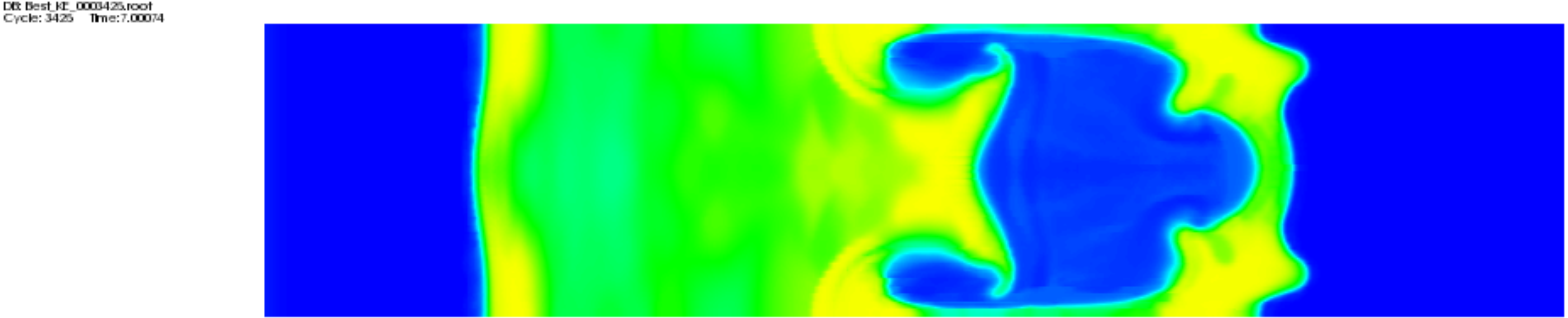
DB: Best_KE_0003425.root
Cycle: 3425 Time:7.00074

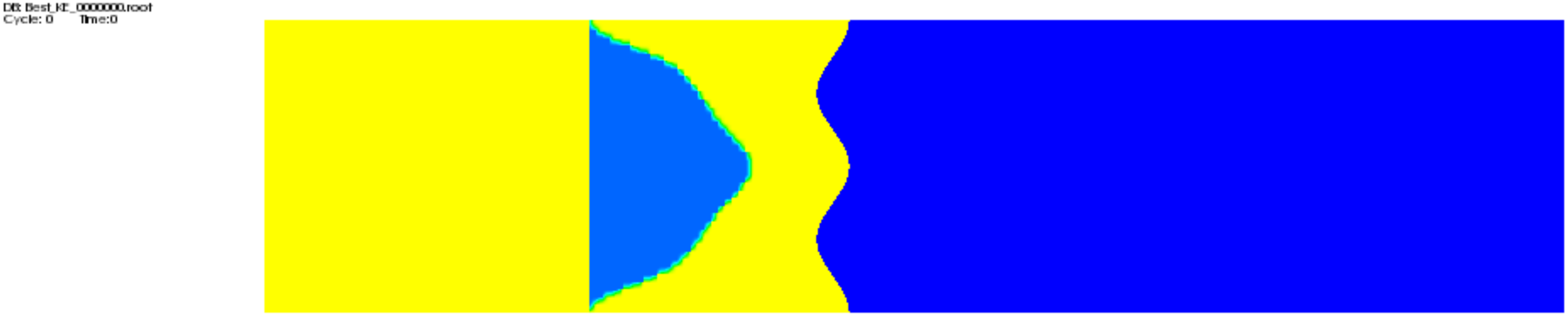
DB: Best_KE_0000000.root
Cycle: 0 Time:0

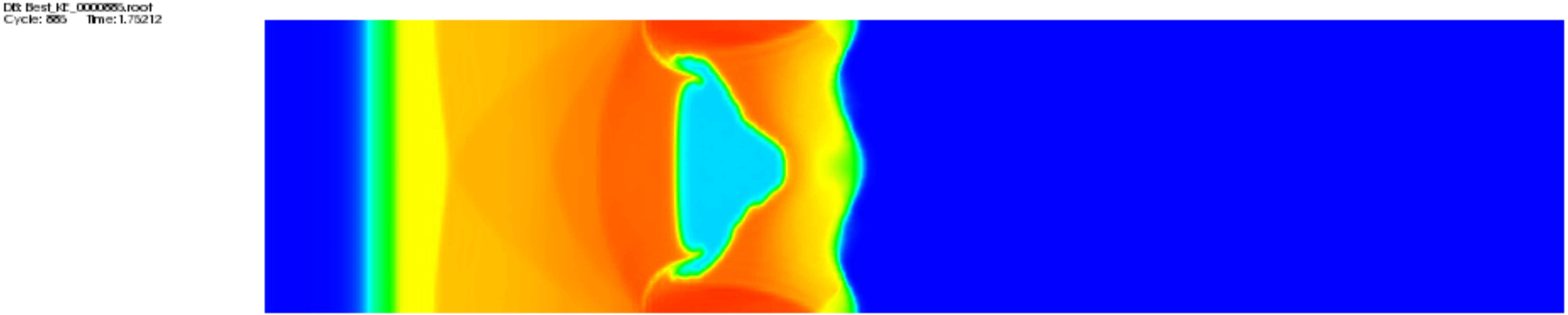
DB: Best_KE_0000885.root
Cycle: 885 Time: 1.75212

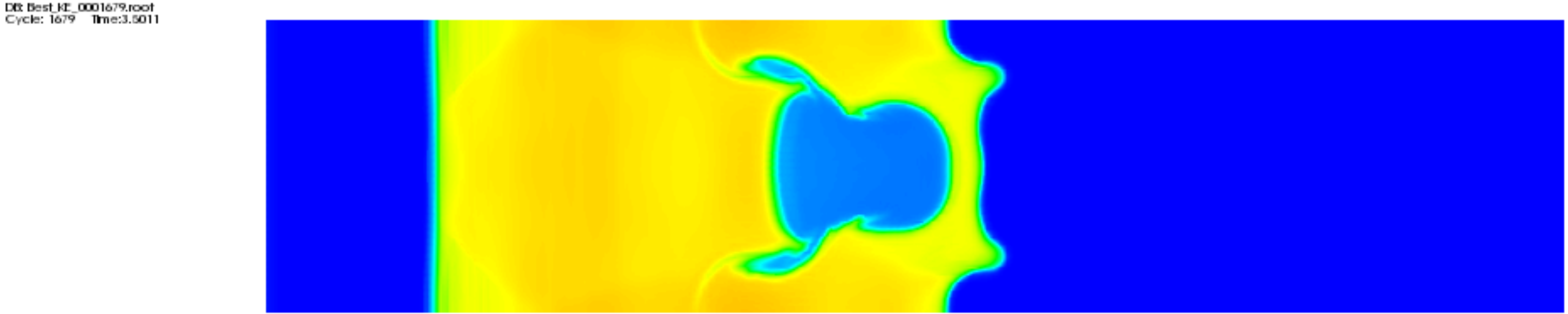
DB: Best_KE_0001679.root
Cycle: 1679 Time:3.5011

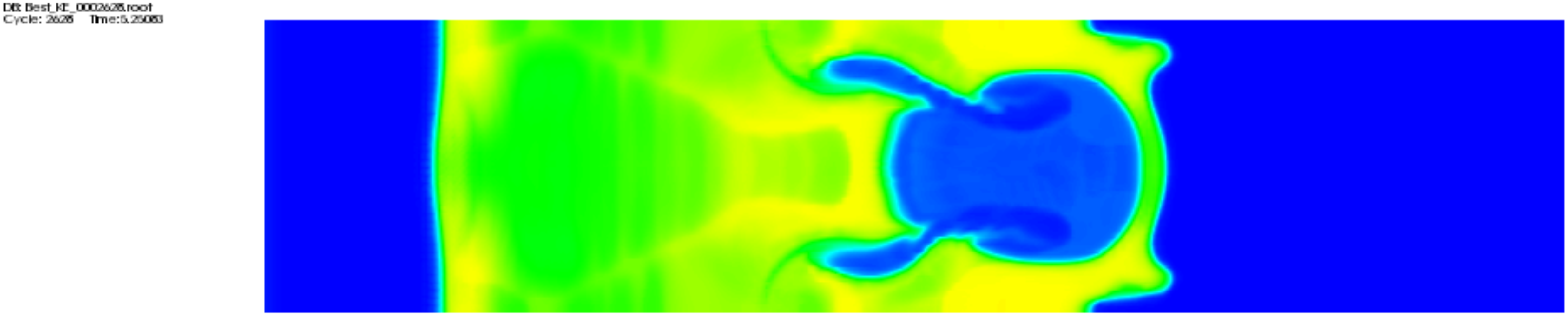
DB: Best_KE_00002628.root
Cycle: 2628 Time:5.25083

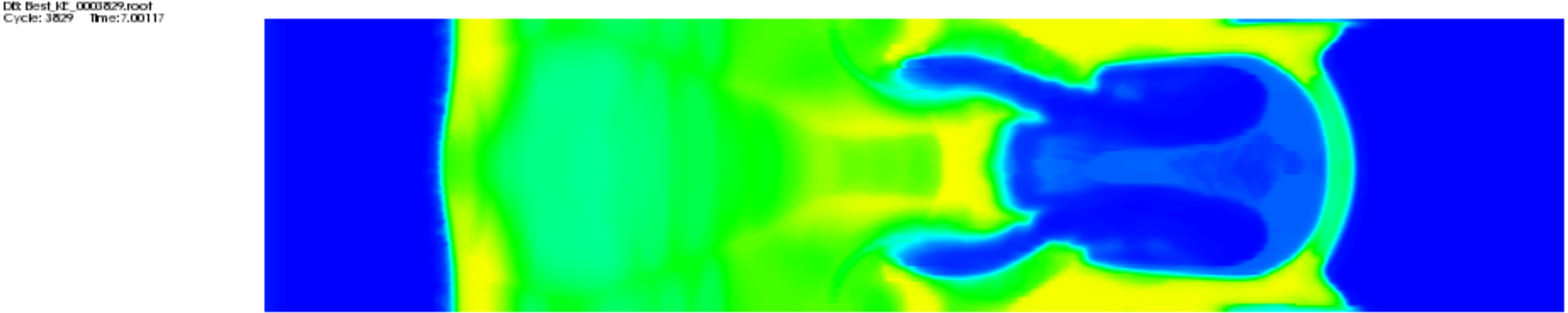
DB: Best_KE_0003829.root
Cycle: 3829 Time:7.00117

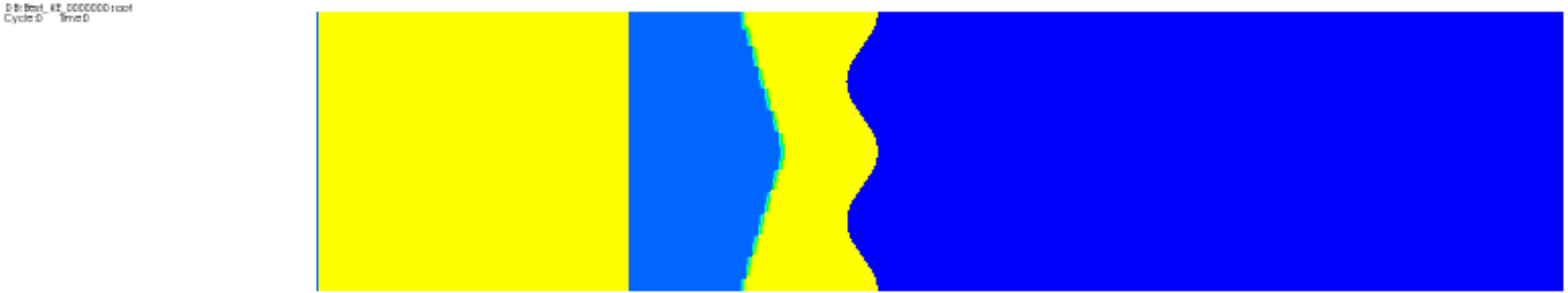
DB: Best_KE_0000000.root
Cycle: 0 Time:0

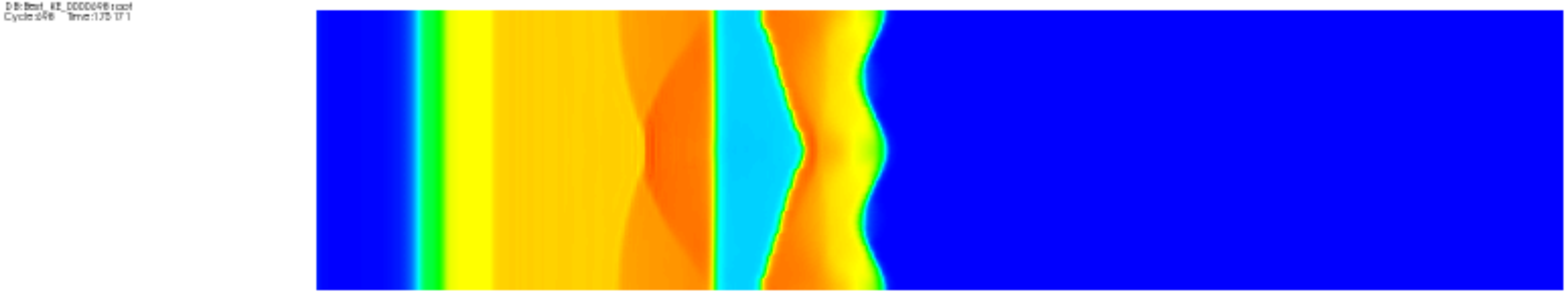
DB: Best_KE_0000698.root
Cycle: 698 Time: 175.171

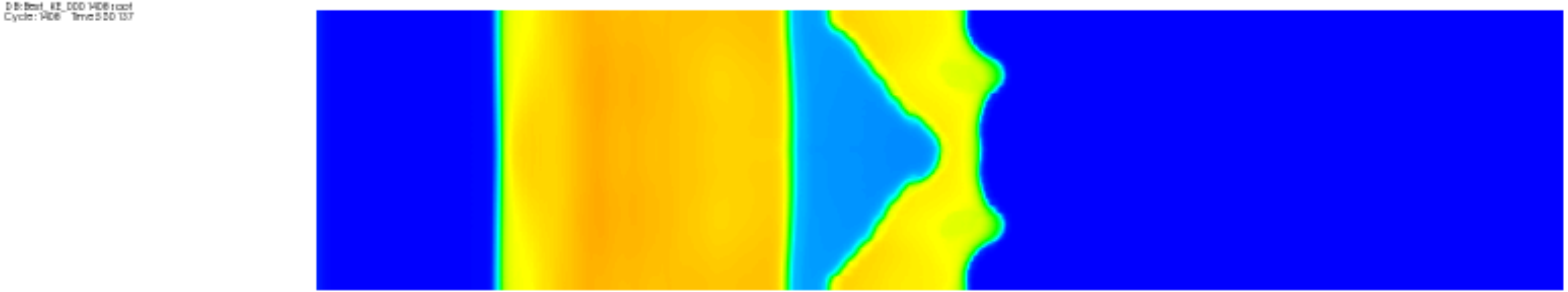
DB: Best_KE_0001406.root
Cycle: 1406   Time:550.137

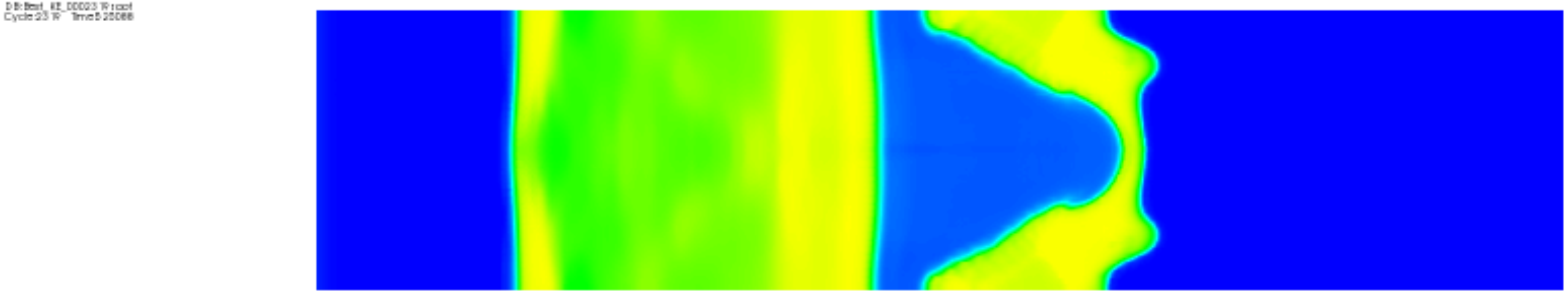
DB: Best_KE_00023.Vr root
Cycle:23 Tr Time:5.25066

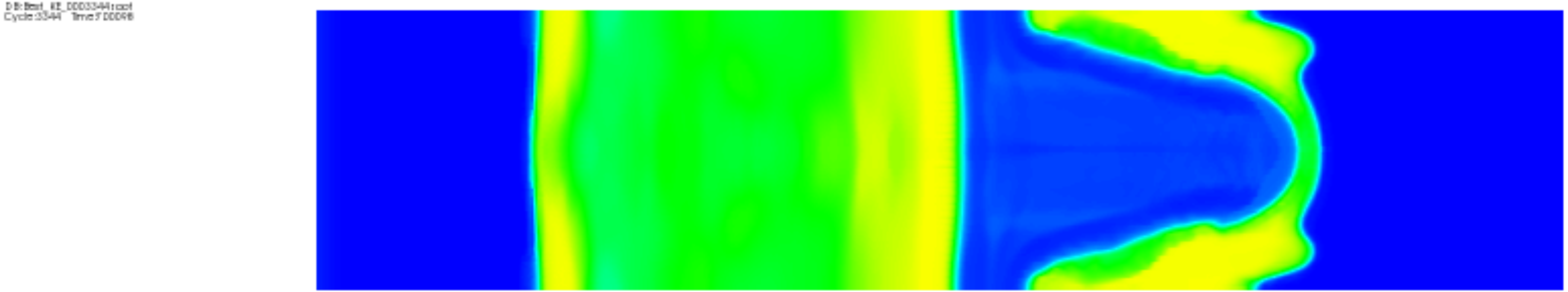
DB: Best_KE_00003344.root
Cycle: 3344 Time: 5.00098

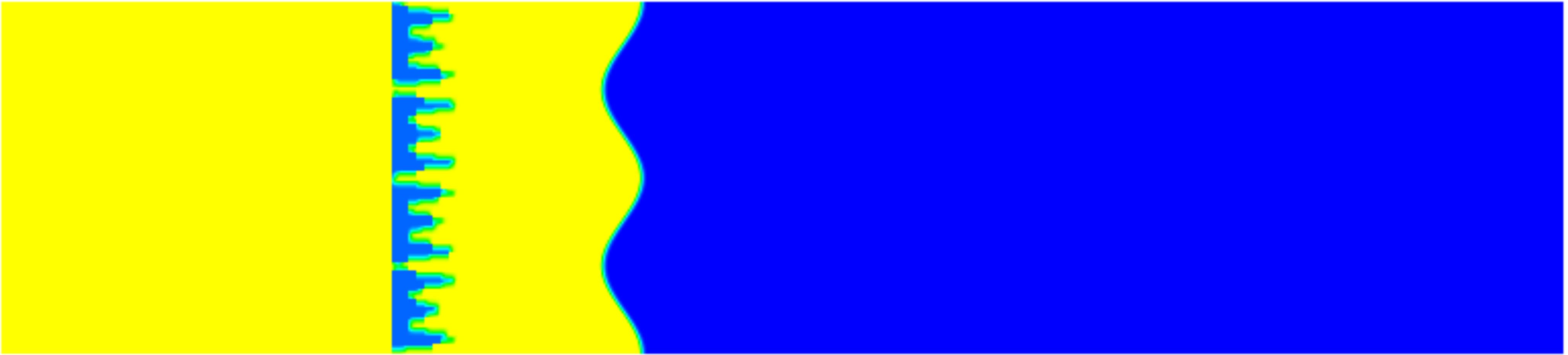

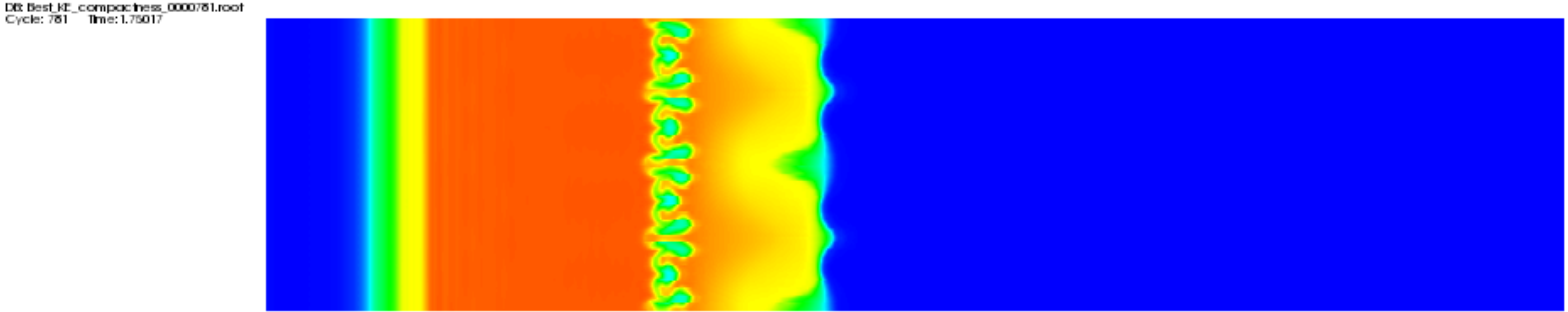
DB: Best_KE_compactness_0000781.root
Cycle: 781 Time: 1.75017

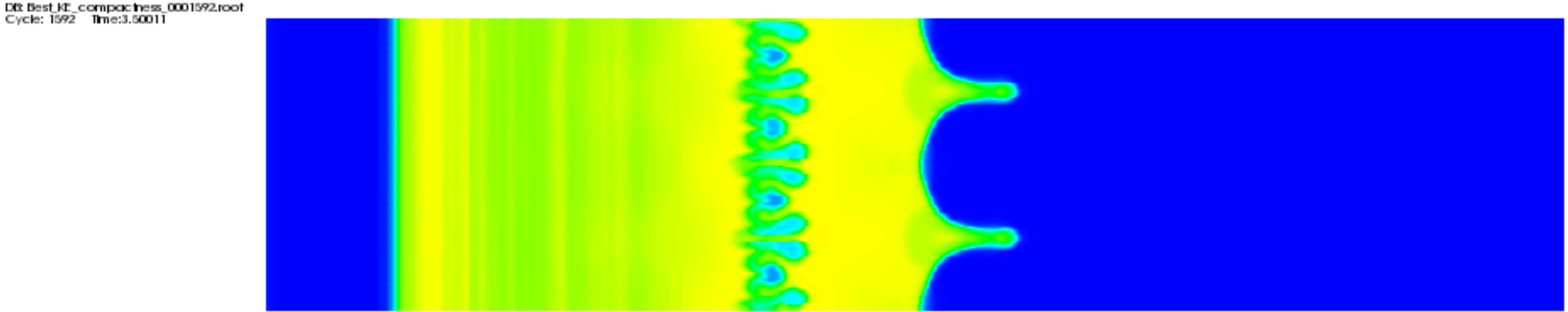
DB: Best_KE_compactness_0001592.root
Cycle: 1592 Time:3.50011

DB: Best_KE_compactness_0002497.root
Cycle: 2497 Time:5.25167

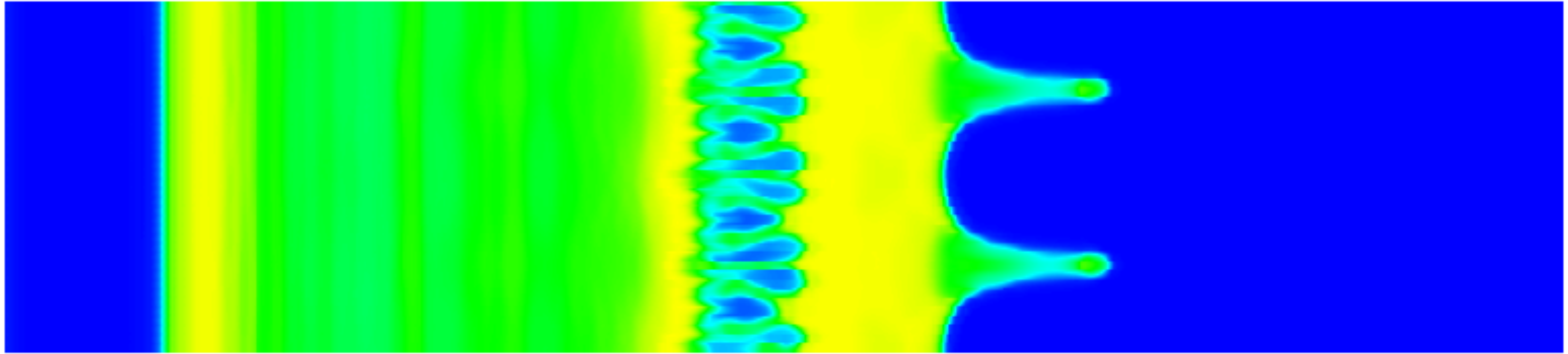

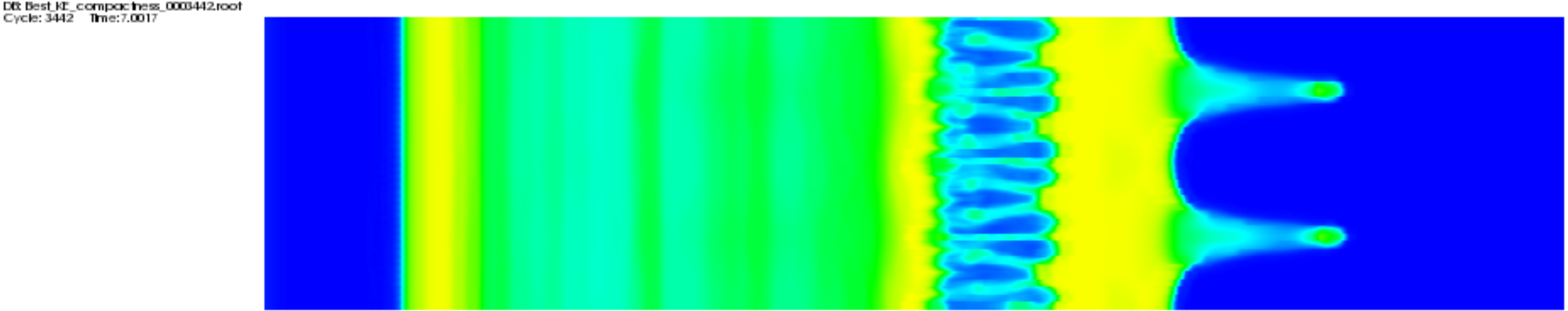
DB: Best_KE_compactness_0003442.root
Cycle: 3442 Time:7.0017

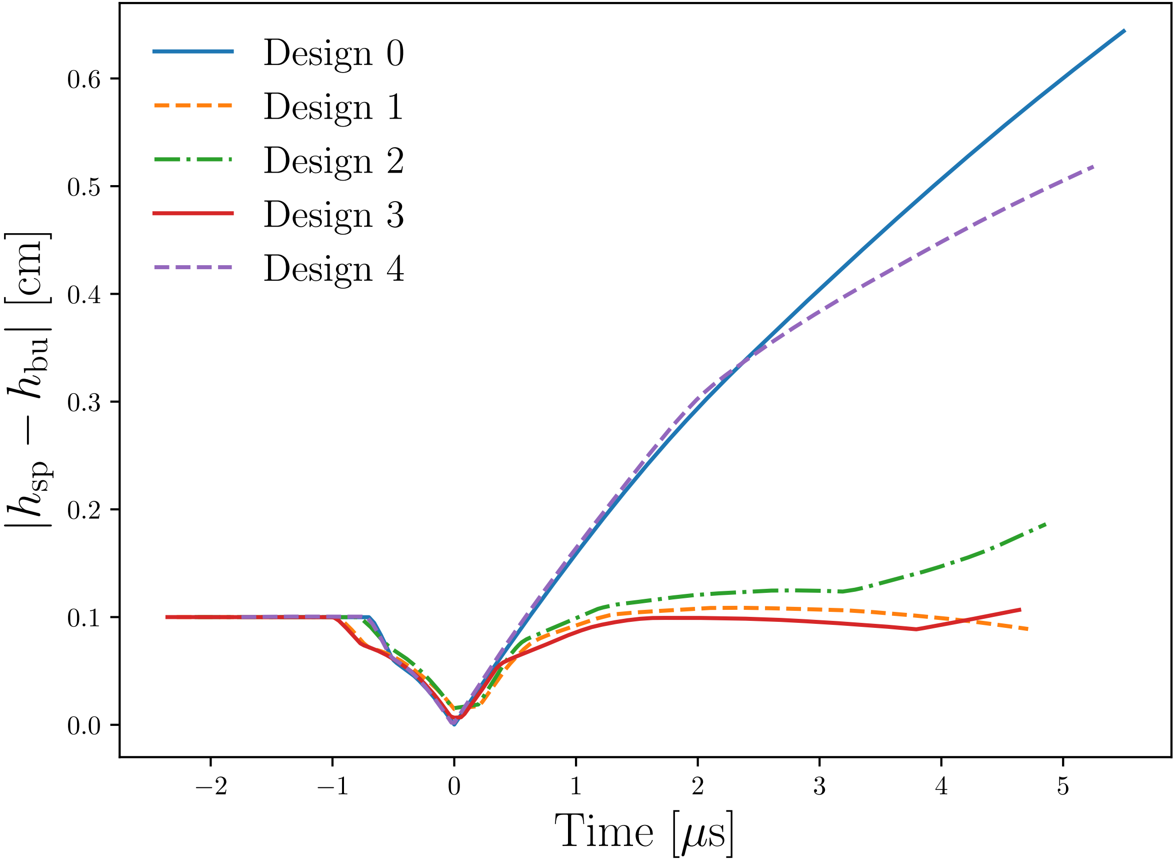
Design 0
Design 1
Design 2
Design 3
Design 4
$|h_{\rm sp} - h_{\rm bu}|$ [cm]
0.0
0.1
0.2
0.3
0.4
0.5
0.6
Time [μs]
−2
−1
0
1
2
3
4
5

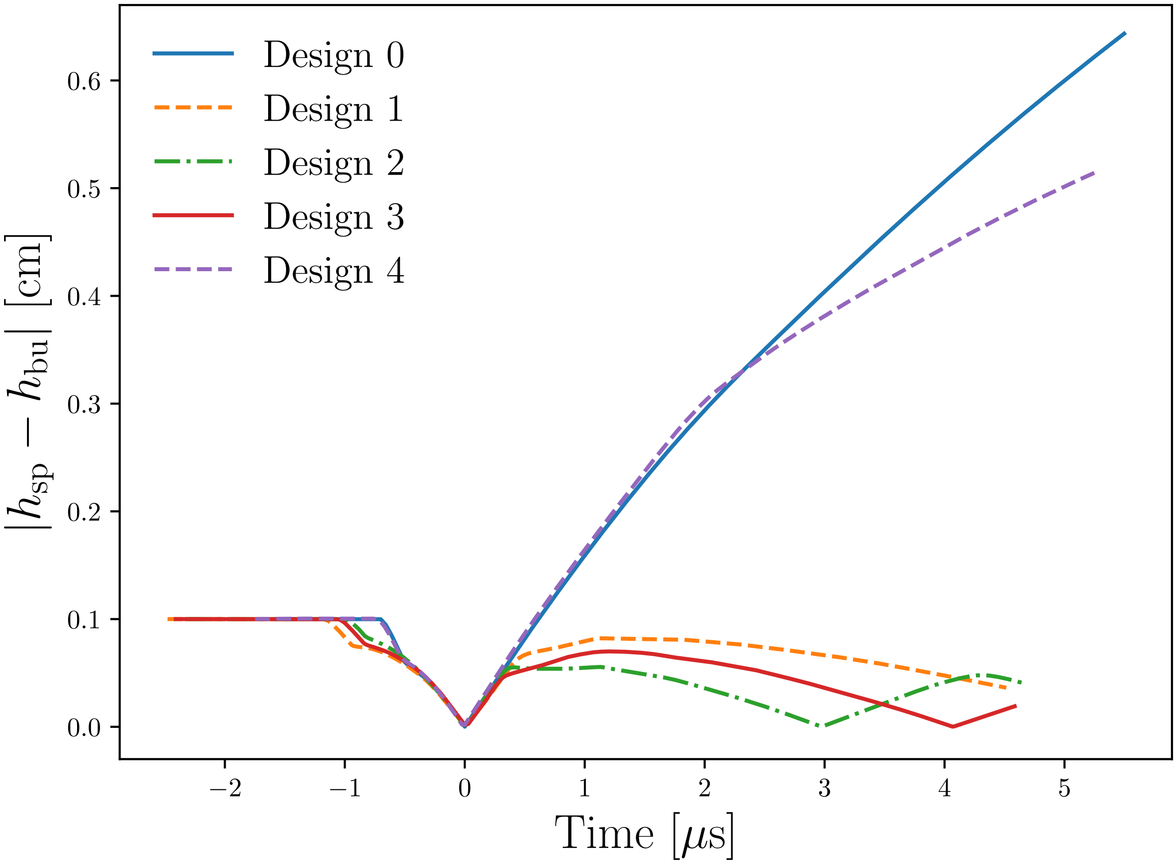
Design 0
Design 1
Design 2
Design 3
Design 4
$|h_{\mathrm{sp}} - h_{\mathrm{bu}}|$ [cm]
0.0
0.1
0.2
0.3
0.4
0.5
0.6
−2
−1
0
1
2
3
4
5
Time [μs]

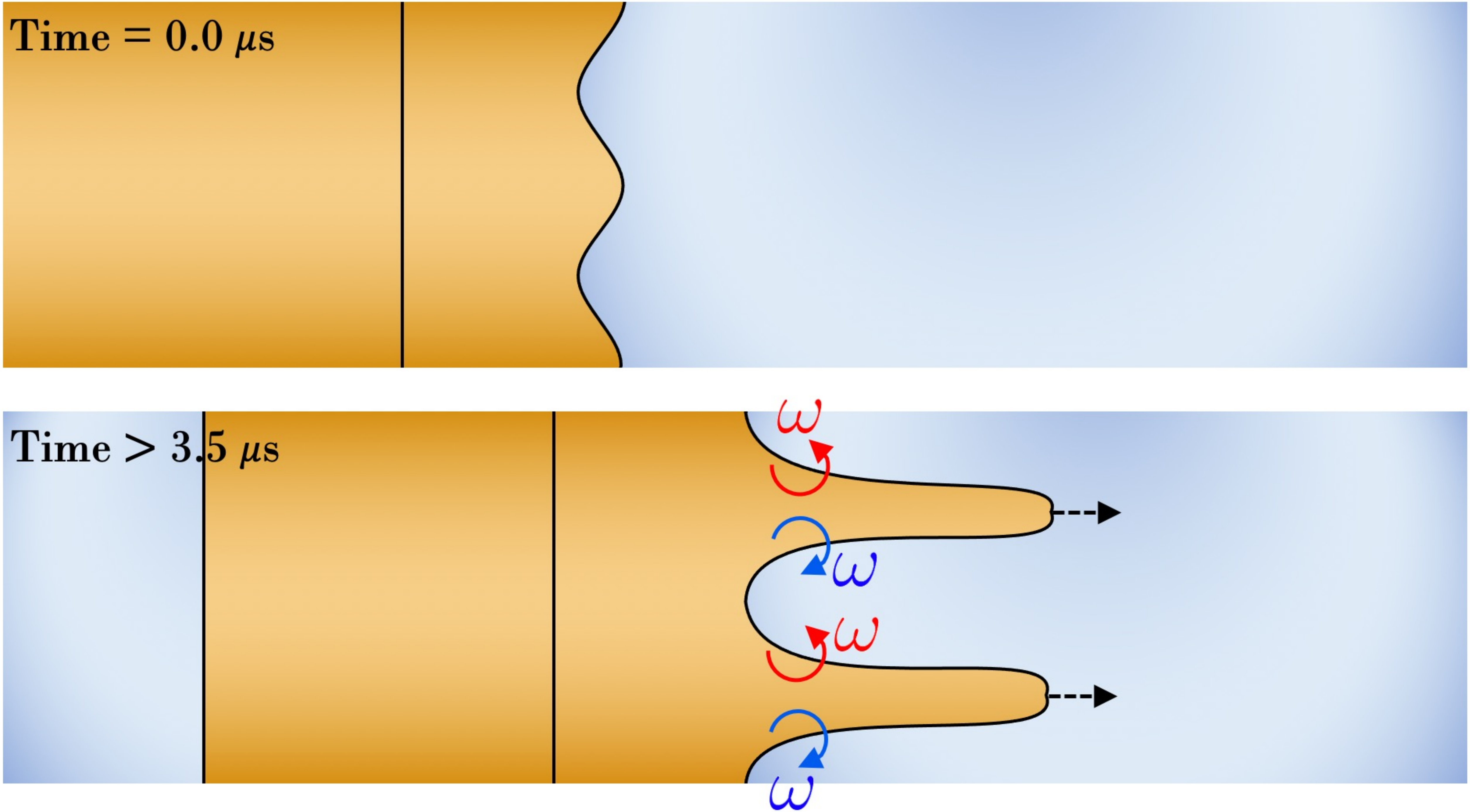
Time = 0.0 μs
Time > 3.5 μs
ω
ω
ω
ω

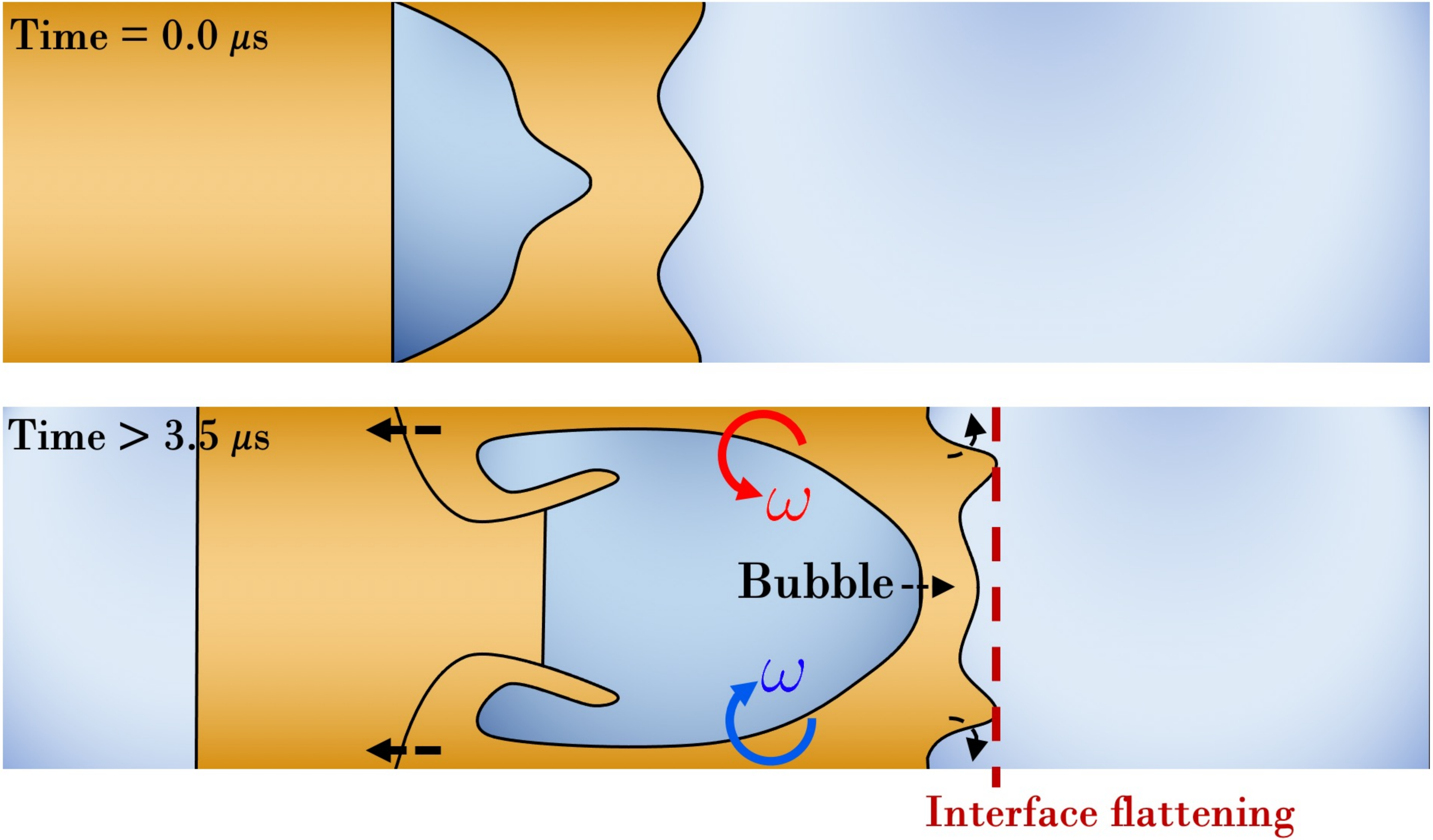
Time = 0.0 μs
Time > 3.5 μs
ω
ω
Bubble
Interface flattening

DB: Best_KE_0000000.root
Cycle: 0 Time:0

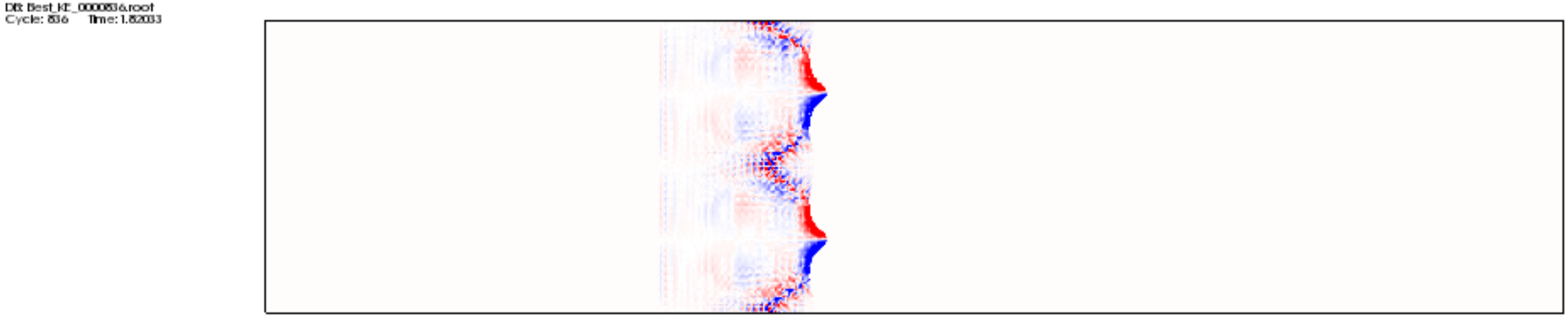
DB: Best_KE_0000836.root
Cycle: 836 Time: 1.82033

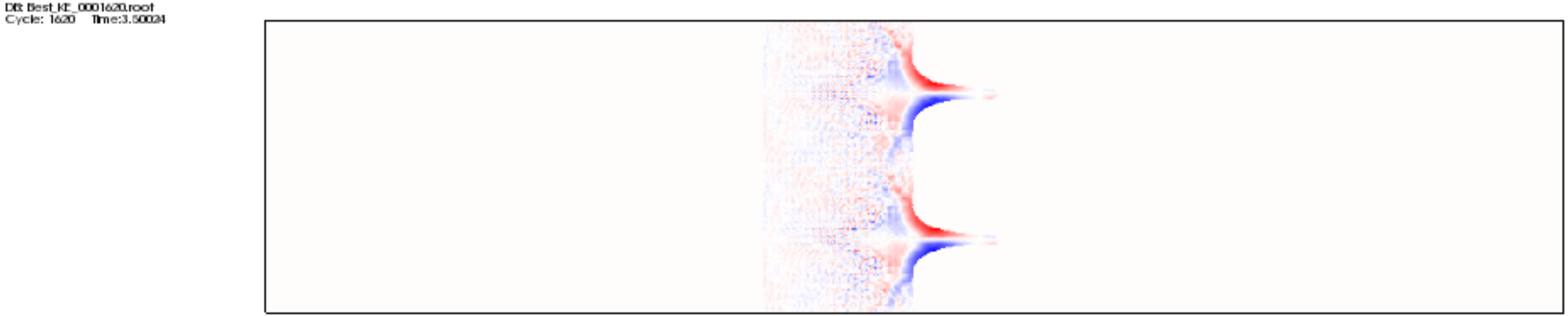
DB: Best_KE_0001620.root
Cycle: 1620 Time:3.50024

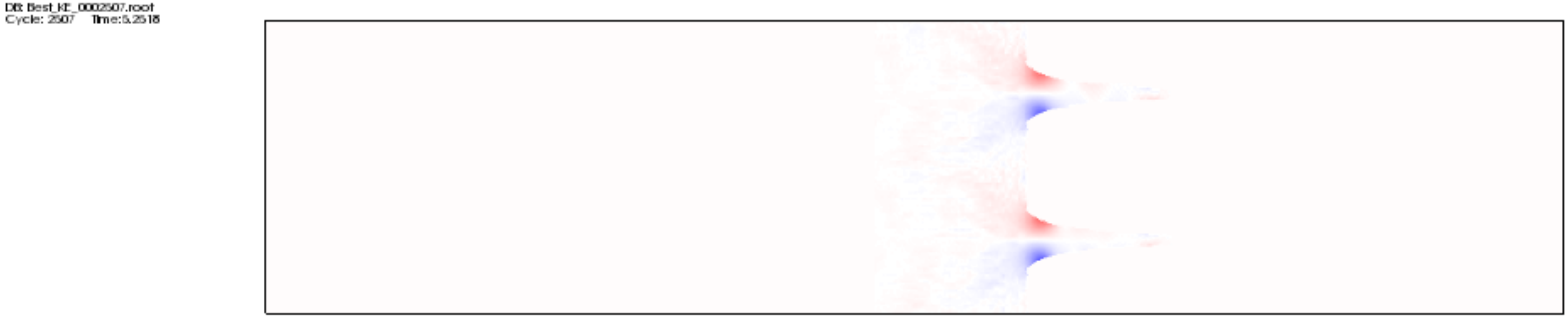
DB: Best_KE_0002507.root
Cycle: 2507 Time:5.2518

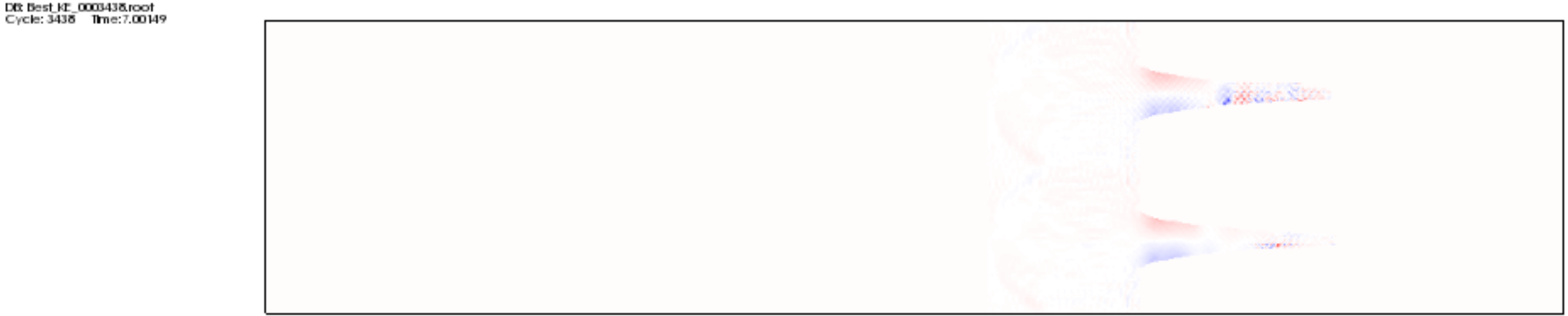
DB: Best_KE_0003438.root
Cycle: 3438 Time:7.00149

DB: Best_KE_0000712.root
Cycle: 712 Time:0.750062
Pseudocolor
Var:blast_mesh/pressure
0.7000
0.5250
0.3500
0.1750
0.000
Max: 0.6787
Min: -0.09674
Contour
Var:blast_mesh/materials
All

DB: Best_KE_0000984.root
Cycle: 984 Time:1.00104
Pseudocolor
Var:blast_mesh/pressure
0.7000
0.5250
0.3500
0.1750
0.000
Max: 1.122
Min: -0.2179
Contour
Var:blast_mesh/materials
All

DB: Best_KE_0001102.root
Cycle: 1102 Time:1.2503
Pseudocolor
Var:blast_mesh/pressure
0.7000
0.5250
0.3500
0.1750
0.000
Max: 0.6041
Min: -0.1155
Contour
Var:blast_mesh/materials
All

DB: Best_KE_0001630.root
Cycle: 1630 Time:1.75076
Pseudocolor
Var:blast_mesh/pressure
0.7000
0.5250
0.3500
0.1750
0.000
Max: 0.6949
Min: -0.04635
Contour
Var:blast_mesh/materials
All

DB: Best_KE_0001998.root
Cycle: 1998 Time:2.25075
Pseudocolor
Var:blast_mesh/pressure
0.7000
0.5250
0.3500
0.1750
0.000
Max: 0.6772
Min: -0.08255
Contour
Var:blast_mesh/materials
All

DB: Best_KE_0000000.root
Cycle: 0 Time:0

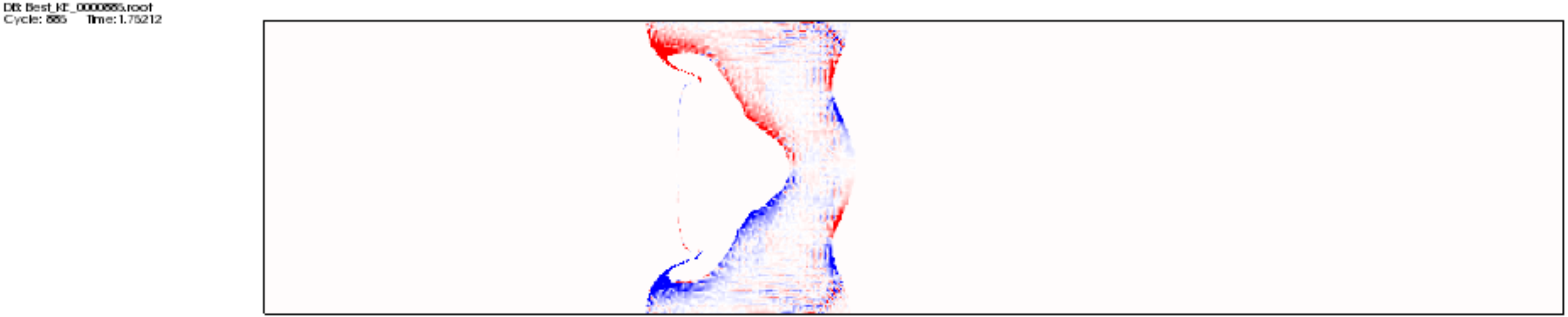
DB: Best_KE_0000885.root
Cycle: 885 Time: 1.75212

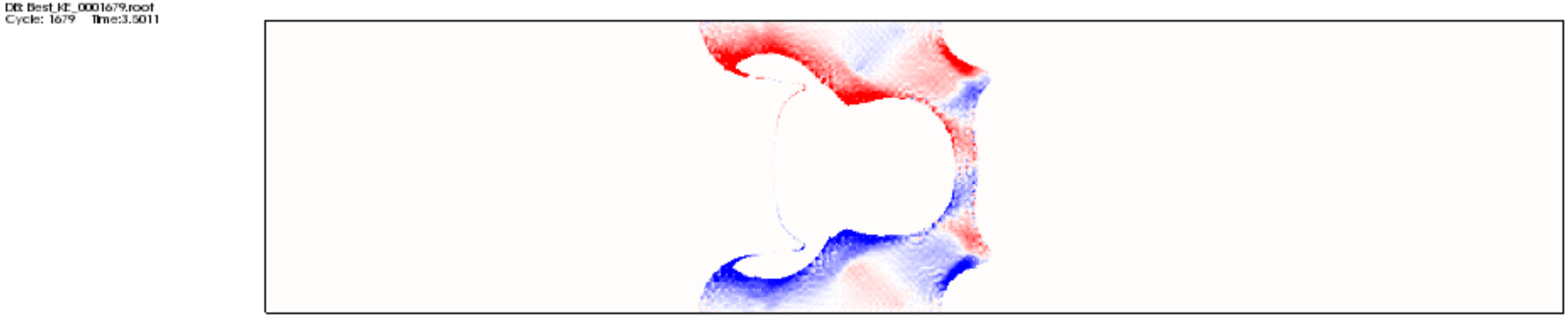
DB: Best_KE_0001679.root
Cycle: 1679 Time:3.5011

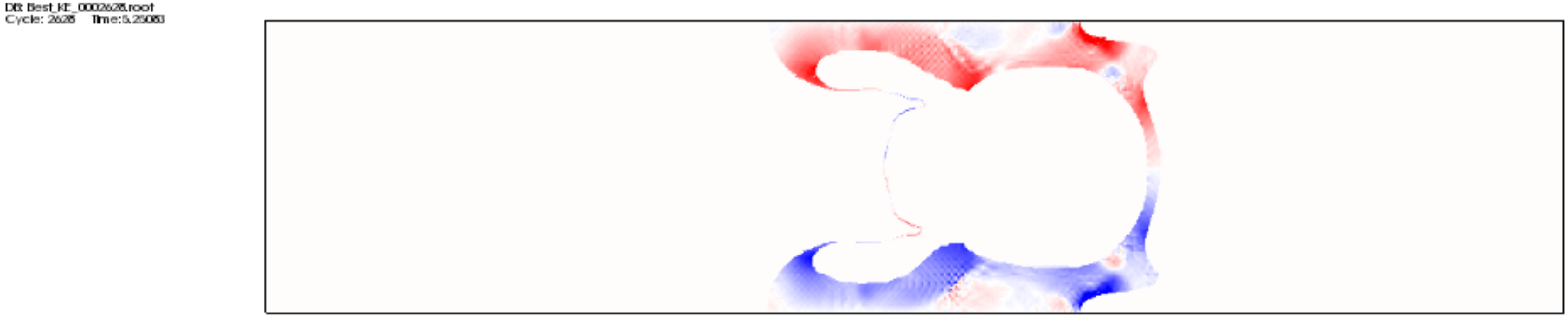
DB: Best_KE_00002628.root
Cycle: 2628 Time:5.25083

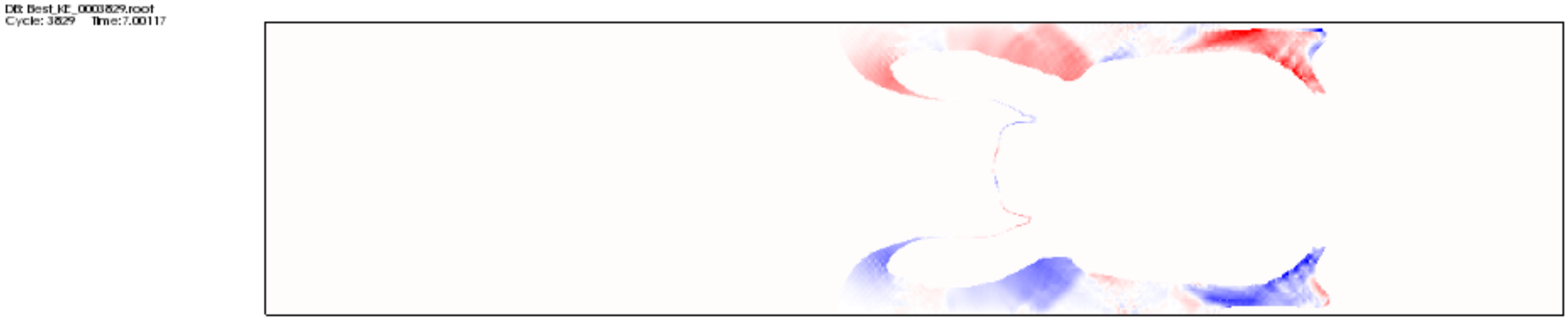
DB: Best_KE_0003829.root
Cycle: 3829 Time:7.00117

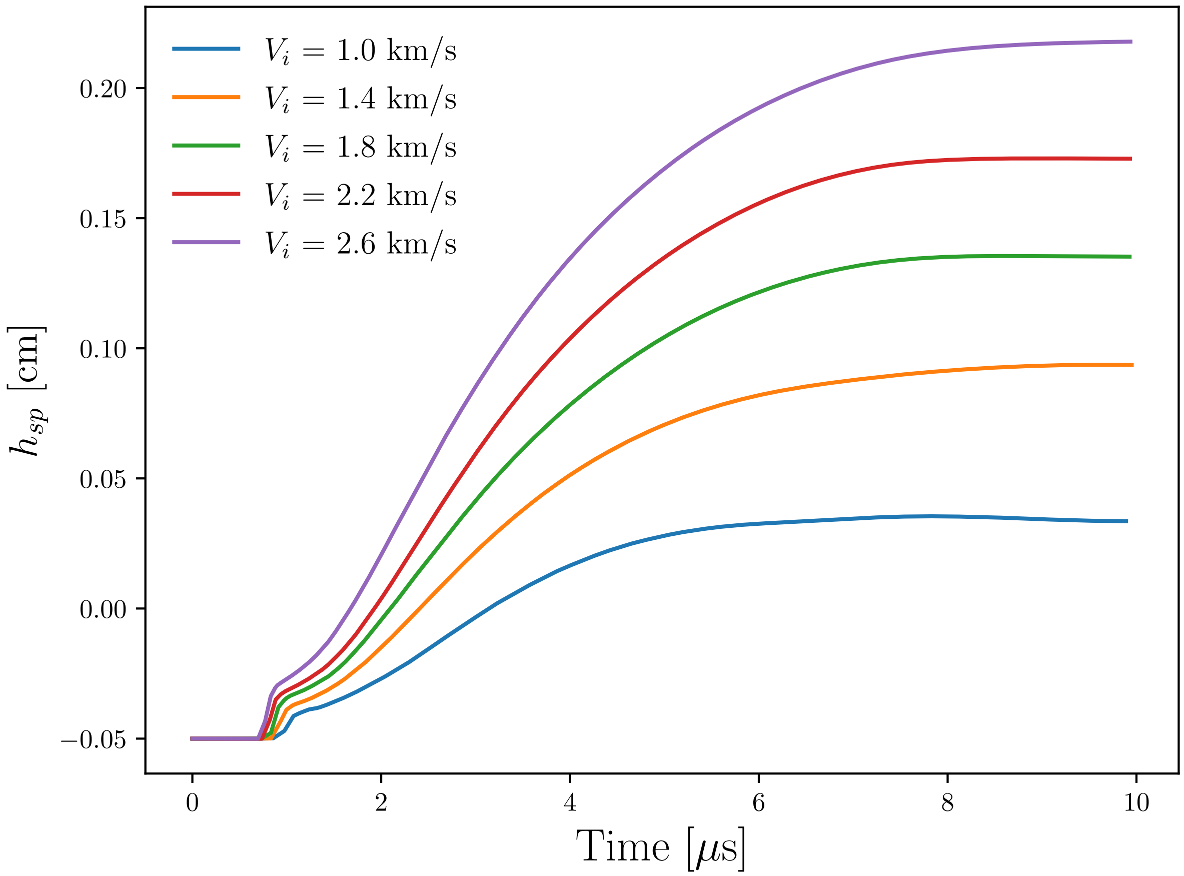
$V_i = 1.0$ km/s
$V_i = 1.4$ km/s
$V_i = 1.8$ km/s
$V_i = 2.2$ km/s
$V_i = 2.6$ km/s
h_{sp} [cm]
0.20
0.15
0.10
0.05
0.00
-0.05
0
2
4
6
8
10
Time [μs]

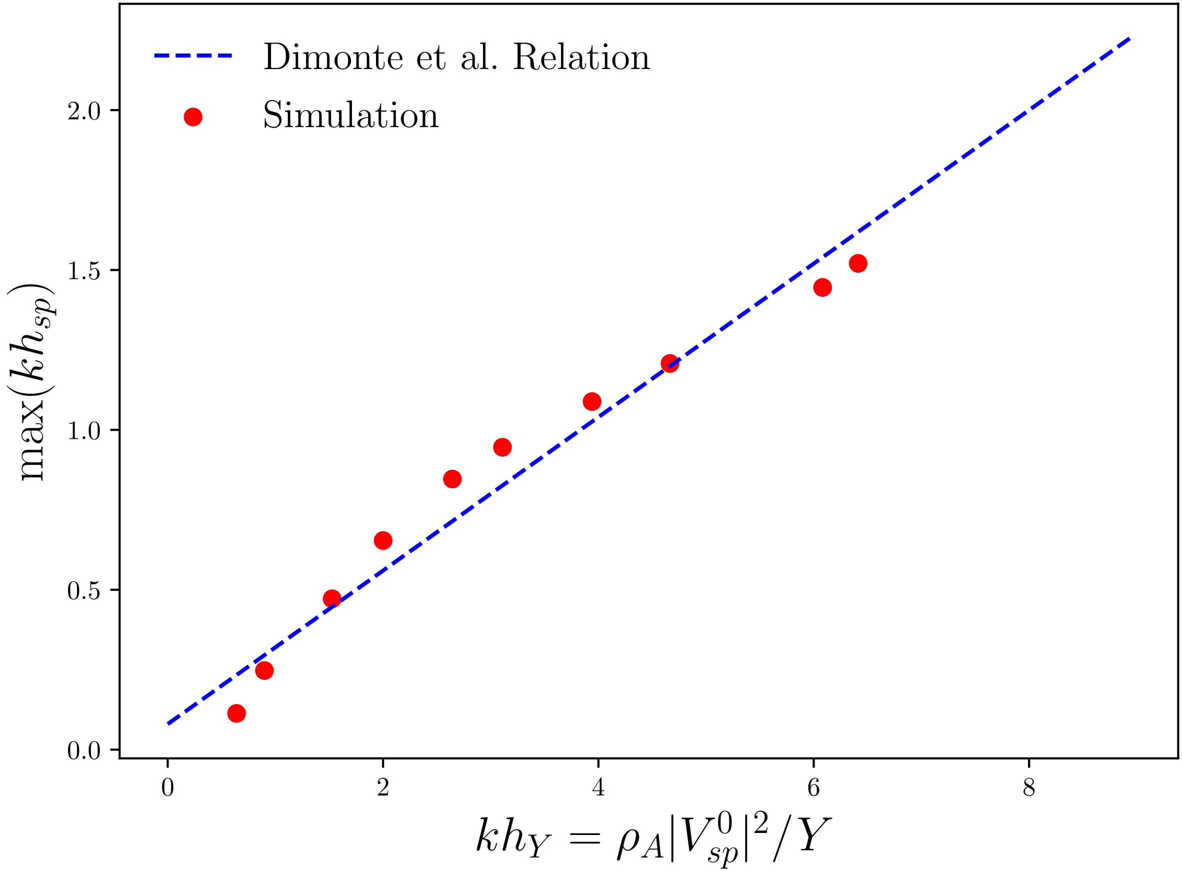
Dimonte et al. Relation
Simulation
$\max(kh_{sp})$
2.0
1.5
1.0
0.5
0.0
0
2
4
6
8
$kh_Y = \rho_A |V_{sp}^0|^2 / Y$

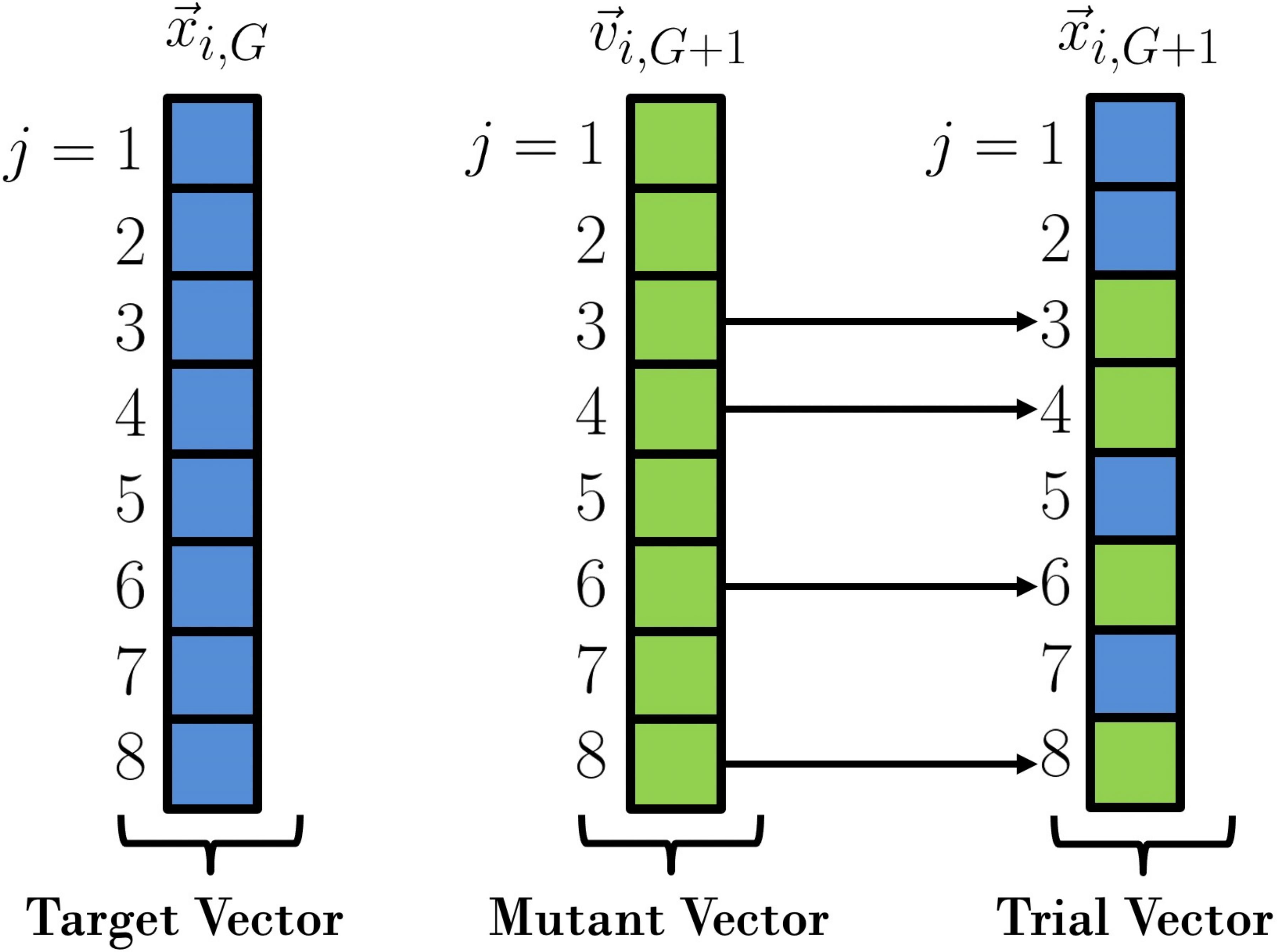
$\vec{x}_{i,G}$
$\vec{v}_{i,G+1}$
$\vec{x}_{i,G+1}$
$j = 1$
$j = 1$
$j = 1$
Target Vector
Mutant Vector
Trial Vector